

# A Multiscale Method Based on the Fibre Configuration Field, IRBF and DAVSS for the Simulation of Fibre Suspension Flows

H.Q. Nguyen<sup>1</sup>, C.-D. Tran<sup>1</sup> and T. Tran-Cong<sup>1</sup>

**Abstract:** In this paper, an Integrated Radial Basis Function (IRBF)-based multiscale method is used to simulate the rheological properties of dilute fibre suspensions. For the approach, a fusion of the IRBF computation scheme, the Discrete Adaptive Viscoelastic Stress Splitting (DAVSS) technique and the Fibre Configuration Field has been developed to investigate the evolution of the flow and the fibre configurations through two separate computational processes. Indeed, the flow conservation equations, which are expressed in vorticity-stream function formulation, are solved using IRBF-based numerical schemes while the evolution of fibre configuration fields governed by the Jeffery's equation is captured using the principle of Brownian Configuration Fields. The two procedures are coupled together by the Lipscomb expression which is used to determine the fibre stress of dilute fibre suspensions. Owing to advantages of the IRBF scheme and the DAVSS technique, the present method yields a more accurate solution and faster convergence rate. The simulation method is verified and its capability is demonstrated with the fibre suspension flows through two parallel plates, a circular tube and the 4:1 and 4.5:1 axisymmetric contraction geometries which are usually chosen to test a numerical method because of the challenging nature of these problems.

**Keywords:** Fibre Configuration Field, Integrated Radial Basis Function, Dilute fibre suspension flow, Jeffery equation, Lipscomb model, Discrete adaptive viscoelastic stress splitting, Multiscale simulation method.

## 1 Introduction

Fibre-reinforced composite materials, e.g. polymer matrices strengthened by glass fibres, are popularly used in many important industrial areas because of their advanced mechanical properties such as high strength and stiffness, and low density

---

<sup>1</sup> Computational Engineering and Science Research Centre, Faculty of Health, Engineering and Science, The University of Southern Queensland, Toowoomba, QLD 4350, Australia.

[Folkes (1982)]. These exceptional properties are mostly dominated by the distribution and orientation of fibres existing inside matrices. Hence, a sufficient understanding of the orientation distribution of fibre configurations in the solvent of a moulding process is very important and needs to be carefully investigated using both experimental and numerical approaches. On the numerical simulation, due to the multiphase nature of the materials, various multiscale simulation methods have been developed based on the micro-mechanical characteristics of the materials. For heterogeneous solid materials such as metals/alloys with precipitates/pores or particulate-reinforced composite materials, several different multiscale schemes were devised to predict the effective properties of the materials as reviewed by Wu, Nie, and Yang (2014) while methods based on the Voronoi Cell Finite Elements [Dong and Atluri (2012)] and the Voronoi Cell Boundary Elements [Dong and Atluri (2013)] were developed for heterogeneous materials with voids and/or rigid/elastic inclusions. For the simulation of inhomogeneous suspensions, whose particles may migrate from one region to another, the readers can refer to publications of Phan-Thien, Graham, Altobelli, Abbott, and Mondy (1995) and Fan, Phan-Thien, and Zheng (2000). In this work, we focus on homogeneous materials with the assumption of constant volume fraction on the flow field at all times [Fan (2006)]. One of the most active research trends in this area is to simulate the flow of fibre suspensions in complex geometries, which has been stimulated by Lipscomb, Denn, Hur, and Boger (1988).

We consider rigid cylindrical fibres of the same length and diameter. Fibre suspensions can be classified into three main groups: dilute, semi-dilute and concentrated suspensions based on two basic parameters, the fibre volume fraction  $\phi$  and the aspect ratio  $a_r$  of the fibre (length/diameter). Specifically, a suspension is considered as dilute, semi-dilute or concentrated for the case of  $\phi a_r^2 < 1$ ,  $1 < \phi a_r^2 < a_r$  or  $\phi a_r > 1$ , respectively.

Generally, the physical description of flow and the evolution of fibre configurations poses challenges related to the necessity to take into account the fibre-fibre, fibre-fluid, and fibre-boundary interactions, especially for suspension flows through complex geometries [Lipscomb, Denn, Hur, and Boger (1988)]. For dilute suspensions, the fibre-fibre interaction is neglected and the evolution of the fibre configuration is captured by the Jeffery's motion equation [Jeffery (1922)]. For semi-dilute and concentrated suspensions, the fibre-fibre interaction is significant. Thus, it is necessary to take into consideration this interaction and one possible way is to introduce a diffusion term into Jeffery's equation [Folgar and Tucker (1984)].

From the literature, the simulation of a fibre suspension is basically carried out through the following three steps: (i) Introduce a fibre stress component into the momentum conservation equation to include dynamic effects of fibres on the bulk

properties of the flow; (ii) Apply an appropriate motion equation to describe the evolution of fibre configuration, as stated above, the Jeffery's equation is suitable for dilute suspension whereas the Folgar and Tucker's equation is applicable for semi-dilute and concentrated ones; and (iii) Determine the fibre contribution to stress (named fibre stress tensor) using a relevant constitutive equation as a function of the fibres' orientation.

Since the fibre stress tensor is essentially calculated from the fourth-order orientation tensor  $\langle \mathbf{PPPP} \rangle$ , the basic difference between numerical methods for the simulation of fibre suspensions is the way to handle the fourth-order tensor. There are several approaches to process the fourth-order orientation tensor. One approach is to use a quadratic closure approximation to break the tensor  $\langle \mathbf{PPPP} \rangle$  into two second-order tensors  $\langle \mathbf{PP} \rangle$  [Lipscomb, Denn, Hur, and Boger (1988)]. A full alignment assumption is subsequently applied to calculate these second-order tensors. This approach was employed to successfully simulate fibre suspension flows through axisymmetric contraction and expansion geometries [Lipscomb, Denn, Hur, and Boger (1988); Chiba, Nakamura, and Boger (1990); Baloch and Webster (1995)]. Another one is to directly solve the evolution of the fourth-order tensor as presented in Advani and Tucker III (1987). And last but not least is the Brownian Configuration Field (BCF) approach [Hulsen, Van Heel, and Van Den Brule (1997); Tran-Canh and Tran-Cong (2004)] which was successfully applied to the simulation of fibre suspensions by Fan, Phan-Thien, and Zheng (1999); Lu, Khoo, Dou, Phan-Thien, and Seng Yeo (2006) and Dou, Khoo, Phan-Thien, Yeo, and Zheng (2007). Following the approach, a high number of fibre configurational fields is initiated on each computational node and the fourth-order tensor is averagely calculated.

Recently, the macro-micro multiscale methods based on the differentiated and integrated RBF approximations have been developed to simulate successfully a range of dilute polymer solutions [Tran, Phillips, and Tran-Cong (2009); Tran, An-Vo, Mai-Duy, and Tran-Cong (2011); Nguyen, Tran, and Tran-Cong (2015)]. Owing to the advantages of RBF-based high order approximation schemes, the approach achieved high-order convergence rate and accuracy [Tran, Mai-Duy, Le-Cao, and Tran-Cong (2012); Nguyen, Tran, and Tran-Cong (2015)]. In this paper, one-dimensional IRBF (1D-IRBF) scheme [Mai-Duy, Le-Cao, and Tran-Cong (2008)] is employed to discretise the conservation equations using vorticity-stream function, whereas the fibre configurations governed by Jeffery's equation are processed using BCF approach. In addition, the constitutive equation of Lipscomb is exploited to evaluate the fibre stress tensor.

The paper is organised as follows. The governing equations in the dimensionless form are presented in section 2. Section 3 gives a short review of the DAVSS's formulation introduced in the governing momentum equation. The vorticity-stream

function approach in planar and axisymmetric flow problems are detailed in section 4, where an implementation of DAVSS technique for the axisymmetric geometry is also described. In section 5, the Euler explicit scheme for temporal discretisation of the equation of fibre configuration fields is presented. The semi-implicit schemes followed by the IRBF-based approximation to the governing flow equations are also described. An algorithm is introduced in detail in section 6. Numerical examples and obtained results are discussed in 7. Finally, the work is closed by concluding remarks in section 8.

## 2 Dimensionless governing equations for fibre suspension flow

Consider an isothermal and incompressible flow of fibre suspensions in two-dimensional (2-D) space. The continuity and momentum equations of the flow are given by [Lu, Khoo, Dou, Phan-Thien, and Seng Yeo (2006)]

$$\nabla \cdot \mathbf{u} = 0, \quad (1)$$

$$\frac{\partial \mathbf{u}}{\partial t} + \mathbf{u} \cdot \nabla \mathbf{u} = -\nabla p + \frac{1}{Re} \nabla \cdot \boldsymbol{\tau}_e, \quad (2)$$

where  $t$ ,  $\mathbf{u}$ ,  $p$  and  $\boldsymbol{\tau}_e$  are the time, velocity field, pressure and extra-stress tensor, respectively, and  $Re$  the Reynolds number based on the viscosity  $\eta_0$  of the Newtonian solvent. For fibre suspensions with a Newtonian solvent, the extra-stress tensor ( $\boldsymbol{\tau}_e$ ) consists of two components as follows.

$$\boldsymbol{\tau}_e = \boldsymbol{\tau}_s + \boldsymbol{\tau}_f, \quad (3)$$

where  $\boldsymbol{\tau}_s = 2\mathbf{D}$  and  $\boldsymbol{\tau}_f$  are the stress components contributed by the Newtonian solvent and the suspended fibres, respectively, and  $\mathbf{D} = \frac{1}{2}(\nabla \mathbf{u} + (\nabla \mathbf{u})^T)$  the rate of strain tensor.

There are several models used to calculate the stress contributed by suspended fibres, for example, the Lipscomb model [Lipscomb, Denn, Hur, and Boger (1988)] for dilute suspensions and the Phan-Thien–Graham model [Phan-Thien and Graham (1991)] for semi-dilute and concentrated suspensions. In this paper, the former one is used to investigate the present method in simulations of dilute fibre suspension flows. The Lipscomb model is given by

$$\boldsymbol{\tau}_f = k_f \mathbf{D} : \langle \mathbf{P} \mathbf{P} \mathbf{P} \mathbf{P} \rangle, \quad (4)$$

where  $\mathbf{P}$  is the unit vector representing the orientation of a fibre;  $\langle \mathbf{P} \mathbf{P} \mathbf{P} \mathbf{P} \rangle$  the fourth order orientation tensor or structure tensor; and  $\langle (\cdot) \rangle$  the statistical average of  $(\cdot)$ .

The dimensionless quantity  $k_f$  is the fibre parameter and defined by

$$k_f = \frac{\phi \mu}{\eta_0}, \tag{5}$$

where  $\eta_0$  is the Newtonian fluid viscosity;  $\phi$  the volume fraction of fibres;  $\mu$  the material constant and chosen in the limit of high aspect ratio of fibre as follows [Chiba, Yasuda, and Nakamura (2001)].

$$\mu = \frac{\eta_0 a_r^2}{\ln(a_r)}, \tag{6}$$

where  $a_r$  is the aspect ratio of fibres. Substituting Eq. (6) into Eq. (5) yields

$$k_f = \frac{\phi a_r^2}{\ln(a_r)}. \tag{7}$$

Therefore, the fibre parameter is considered as the only single one in the fibre stress equation (4), which describes the impact of suspended fibres on the kinematic behaviour of the flow.

The evolution of fibres' orientation in flow is captured by the Jeffery's equation as follows [Lipscomb, Denn, Hur, and Boger (1988)].

$$\frac{\partial \mathbf{P}}{\partial t} + \mathbf{u} \cdot \nabla \mathbf{P} = \boldsymbol{\Omega} \cdot \mathbf{P} + \lambda (\mathbf{D} - \mathbf{D} : \mathbf{P} \mathbf{P} \mathbf{I}) \cdot \mathbf{P}, \tag{8}$$

where  $\boldsymbol{\Omega} = \frac{1}{2} \left( (\nabla \mathbf{u})^T - \nabla \mathbf{u} \right)$  is the vorticity tensor;  $\lambda$  a parameter dependent on the aspect ratio,  $\lambda = \frac{a_r^2 - 1}{a_r^2 + 1}$  and  $\mathbf{I}$  the identity matrix. As shown in Phan-Thien and Graham (1991), by introducing

$$\mathbf{Q}(\mathbf{x}, t) = Q \mathbf{P}(\mathbf{x}, t), \tag{9}$$

where  $Q$  is the modulus of  $\mathbf{Q}$ , the Jeffery's equation (8) is transformed into

$$\frac{\partial \mathbf{Q}}{\partial t} + \mathbf{u} \cdot \nabla \mathbf{Q} = (\nabla \mathbf{u})^T \cdot \mathbf{Q} - \zeta \mathbf{D} \cdot \mathbf{Q} \tag{10}$$

where  $\zeta = 2/(a_r^2 + 1) = 1 - \lambda$ . The fourth order orientation tensor  $\langle \mathbf{P} \mathbf{P} \mathbf{P} \mathbf{P} \rangle$  in Eq. (4) can be now defined by

$$\langle \mathbf{P}_i \mathbf{P}_i \mathbf{P}_i \mathbf{P}_i \rangle = \frac{1}{N_f} \sum_{i=1}^{N_f} \left\langle \frac{\mathbf{Q}_i \mathbf{Q}_i \mathbf{Q}_i \mathbf{Q}_i}{Q_i Q_i Q_i Q_i} \right\rangle, \tag{11}$$

where  $N_f$  is the number of fibres. The components of the tensor  $\langle \mathbf{PPPP} \rangle$  in a 2-D fibre orientation field are given by [Chiba, Yasuda, and Nakamura (2001)]

$$P_{1111} = \sum_{i=1}^{N_f} \frac{\cos^4 \theta_i}{N_f}, \quad P_{1112} = \sum_{i=1}^{N_f} \frac{\cos^3 \theta_i \sin \theta_i}{N_f}, \quad P_{1122} = \sum_{i=1}^{N_f} \frac{\cos^2 \theta_i \sin^2 \theta_i}{N_f}, \quad (12)$$

$$P_{1222} = \sum_{i=1}^{N_f} \frac{\cos \theta_i \sin^3 \theta_i}{N_f}, \quad P_{2222} = \sum_{i=1}^{N_f} \frac{\sin^4 \theta_i}{N_f}, \quad (13)$$

where  $\theta_i$  is the angle between the  $x$ -axis and the axis of fibre  $i$ .

### 3 The Discrete Adaptive Viscoelastic Stress Splitting (DAVSS) formulation

The DAVSS scheme has been widely used in numerical methods to maintain the numerical stability for simulations of viscoelastic fluids [Sun, Phan-Thien, and Tanner (1996); Sun, Smith, Armstrong, and Brown (1999)] and fibre suspensions [Fan, Phan-Thien, and Zheng (1999); Lu, Khoo, Dou, Phan-Thien, and Seng Yeo (2006)]. The DAVSS transformation is introduced into the original momentum equation (2) as follows [Fan, Phan-Thien, and Zheng (1999); Lu, Khoo, Dou, Phan-Thien, and Seng Yeo (2006)].

$$\frac{\partial \mathbf{u}}{\partial t} + \mathbf{u} \cdot \nabla \mathbf{u} - \frac{1}{Re} \nabla \cdot \left[ \eta_a \left( \nabla \mathbf{u} + (\nabla \mathbf{u})^T \right) \right] = -\nabla p - \frac{2}{Re} \nabla \cdot [(\eta_a - 1) \mathbf{D}] + \frac{1}{Re} \nabla \cdot \boldsymbol{\tau}_f, \quad (14)$$

where  $\eta_a$  is the adaptive viscosity. For the dilute fibre suspension using Lipscomb model, the adaptive viscosity is a function of fibre stress and given by [Lu, Khoo, Dou, Phan-Thien, and Seng Yeo (2006)]

$$\eta_a = k_f + \frac{1 + \sqrt{(1/2) \boldsymbol{\tau}_f : \boldsymbol{\tau}_f}}{1 + \sqrt{2 \mathbf{D} : \mathbf{D}}}, \quad (15)$$

where  $k_f$  is the fibre parameter. It is worth noting that there are several differences appearing in the second term of the right-hand-side of Eq. (14) and in the denominator of the second term in Eq. (15) as compared with ones mentioned in Fan, Phan-Thien, and Zheng (1999) and Lu, Khoo, Dou, Phan-Thien, and Seng Yeo (2006). These differences happen because the strain rate tensor  $\mathbf{D}$  is here defined as  $\frac{1}{2} \left( \nabla \mathbf{u} + (\nabla \mathbf{u})^T \right)$ , instead of  $\left( \nabla \mathbf{u} + (\nabla \mathbf{u})^T \right)$  as presented in the cited papers. Furthermore, in this work, the DAVSS formulation is only applied to simulate fibre suspensions in axisymmetric flows but not in the planar Poiseuille one whose geometry is quite simple.

#### 4 Vorticity-stream function formulation for 2-D flows

For 2-D problems considered in this work, it is more convenient to use the vorticity-stream function formulation which offers several numerical benefits as (i) the continuity equation is automatically satisfied; and (ii) the pressure field disappears in the equation of motion.

##### 4.1 Vorticity-stream function formulation in the 2-D Cartesian coordinates $(x, y)$

The relations between velocity  $(u, v)$ , vorticity  $\omega$  and stream function  $\Psi$  are given by

$$\omega = \frac{1}{2} \left( \frac{\partial u}{\partial y} - \frac{\partial v}{\partial x} \right), \tag{16}$$

$$u = \frac{\partial \Psi}{\partial y}, \quad v = -\frac{\partial \Psi}{\partial x}. \tag{17}$$

Substituting the expressions in Eq. (17) into Eq. (16) yields the following vorticity-stream function formulation

$$\frac{\partial^2 \Psi}{\partial x^2} + \frac{\partial^2 \Psi}{\partial y^2} = 2\omega. \tag{18}$$

Taking the curl of Eq. (2) and using Eqs. (1), (3) - (16), the vorticity transport equation is written as follows.

$$\frac{\partial \omega}{\partial t} + u \frac{\partial \omega}{\partial x} + v \frac{\partial \omega}{\partial y} = \frac{1}{Re} \left( \frac{\partial^2 \omega}{\partial x^2} + \frac{\partial^2 \omega}{\partial y^2} \right) + \frac{1}{2Re} \left( \frac{\partial^2 \tau_f^{xx}}{\partial x \partial y} + \frac{\partial^2 \tau_f^{xy}}{\partial y^2} - \frac{\partial^2 \tau_f^{yx}}{\partial x^2} - \frac{\partial^2 \tau_f^{yy}}{\partial x \partial y} \right), \tag{19}$$

where  $\tau_f^{xx}$ ,  $\tau_f^{xy}$ ,  $\tau_f^{yx}$  and  $\tau_f^{yy}$  are the stress components of the symmetric fibre stress tensor  $\boldsymbol{\tau}_f$ .

##### 4.2 Axisymmetric vorticity-stream function formulation in the cylindrical coordinates $(r, z)$

The considered flow is predominantly in the  $z$ -direction and the relations between velocity  $(u_r, u_z)$ , vorticity  $\omega$ , and stream function  $\Psi$  are given by

$$\omega = \frac{1}{2} \left( \frac{\partial u_z}{\partial r} - \frac{\partial u_r}{\partial z} \right), \tag{20}$$

$$u_z = \frac{1}{r} \frac{\partial \Psi}{\partial r}, \quad u_r = -\frac{1}{r} \frac{\partial \Psi}{\partial z}. \tag{21}$$

Following manipulation as done in section 4.1, the vorticity transport and stream function equations are given by

$$\frac{\partial \omega}{\partial t} + u_z \frac{\partial \omega}{\partial z} + u_r \frac{\partial \omega}{\partial r} - \frac{u_r}{r} \omega = \frac{1}{Re} \left( \frac{\partial^2 \omega}{\partial z^2} + \frac{\partial^2 \omega}{\partial r^2} + \frac{1}{r} \frac{\partial \omega}{\partial r} - \frac{1}{r^2} \omega \right) + \frac{1}{2Re} \left( \frac{\partial^2 \tau_f^{rz}}{\partial r^2} - \frac{\partial^2 \tau_f^{rz}}{\partial z^2} + \frac{\partial^2 \tau_f^{zz}}{\partial r \partial z} - \frac{\partial^2 \tau_f^{rr}}{\partial z \partial r} + \frac{1}{r} \frac{\partial \tau_f^{rz}}{\partial r} - \frac{1}{r} \frac{\partial \tau_f^{rr}}{\partial z} - \frac{1}{r^2} \tau_f^{rz} \right), \tag{22}$$

$$\frac{1}{r} \frac{\partial^2 \Psi}{\partial z^2} + \frac{1}{r} \frac{\partial^2 \Psi}{\partial r^2} - \frac{1}{r^2} \frac{\partial \Psi}{\partial r} = 2\omega, \tag{23}$$

where  $\tau_f^{zz}$ ,  $\tau_f^{zr}$ ,  $\tau_f^{rz}$  and  $\tau_f^{rr}$  are the stress components of the fibre stress tensor  $\boldsymbol{\tau}_f$ .

The vorticity transport equation (22) is rewritten with the implementation of DAVSS as follows.

$$\frac{\partial \omega}{\partial t} + u_z \frac{\partial \omega}{\partial z} + u_r \frac{\partial \omega}{\partial r} - \frac{u_r}{r} \omega - \frac{1}{Re} \eta_a \left( \frac{\partial^2 \omega}{\partial z^2} + \frac{\partial^2 \omega}{\partial r^2} \right) = -\frac{1}{Re} (\eta_a - 1) \cdot \left( \frac{\partial^2 \omega}{\partial z^2} + \frac{\partial^2 \omega}{\partial r^2} \right) + \frac{1}{Re} \left( \frac{1}{r} \frac{\partial \omega}{\partial r} - \frac{1}{r^2} \omega \right) + \frac{1}{2Re} \left( \frac{\partial^2 \tau_f^{rz}}{\partial r^2} - \frac{\partial^2 \tau_f^{rz}}{\partial z^2} + \frac{\partial^2 \tau_f^{zz}}{\partial r \partial z} - \frac{\partial^2 \tau_f^{rr}}{\partial z \partial r} + \frac{1}{r} \frac{\partial \tau_f^{rz}}{\partial r} - \frac{1}{r} \frac{\partial \tau_f^{rr}}{\partial z} - \frac{1}{r^2} \tau_f^{rz} \right), \tag{24}$$

where  $\eta_a$  is the adaptive viscosity and given in Eq. (15).

## 5 Numerical method

In this work, the fusion of IRBF and DAVSS is used to simulate fibre suspension flows, in which a semi-implicit scheme is applied to temporally discretise the vorticity transport equations (19) and (24) while the Euler explicit scheme is used for the equation of fibre configuration fields (9). At each time step, the 1D-IRBF scheme is employed to approximate both the field variables of flow and the fibre stress tensor.

**5.1 Temporal discretisation of the vorticity transport equation and the equation of fibre configuration fields**

Consider a time dependent differential equation together with its initial and boundary conditions as follows.

$$\frac{\partial \omega(x,t)}{\partial t} + \mathcal{L} \omega(x,t) = f, \quad (x,t) \in \Gamma \times [0, T] \tag{25}$$

$$\omega(x,t) = g, \quad (x,t) \in \Gamma \times \{0\} \tag{26}$$

$$\mathcal{B} \omega(x,t) = h, \quad (x,t) \in \partial \Gamma \times [0, T], \tag{27}$$

where  $\Gamma$  and  $\partial \Gamma$  are a bounded domain and its boundary, respectively;  $T$  a final time;  $\mathcal{L}$  a differential operator;  $\mathcal{B}$  an operator expressing a boundary condition; and  $f$ ,  $g$  and  $h$  known functions. Assume that the time interval  $[0, T]$  is partitioned into  $N_t$  equal sub-intervals  $[t^n, t^{n+1}]$  of length  $\Delta t$  ( $\Delta t = T/N_t$ ) with  $t^0 = 0$  and  $t^{N_t} = T$ . In fully discrete schemes, Eq. (25) is discretised with respect to both time and space variables. The discretisation in time is accomplished by a time-stepping scheme, followed by the spatial discretisation based on an IRBFN method. Applying the  $\theta$  scheme to Eq. (25) yields

$$\frac{\omega^{n+1} - \omega^n}{\Delta t} + \theta \mathcal{L} \omega^{n+1} + (1 - \theta) \mathcal{L} \omega^n = f, \tag{28}$$

where superscripts  $(n + 1)$  and  $n$  indicates the two successive time steps at  $t^{n+1} = (n + 1)\Delta t$  and  $t^n = n\Delta t$ , respectively;  $\Delta t$  the size of the time step; and  $\omega^n = \omega(x, t^n)$  and  $\omega^{n+1} = \omega(x, t^{n+1})$ . Equation (28) together with the constraint conditions Eq. (26) and Eq. (27) at time  $t^{n+1}$  are then spatially discretised using an IRBF approach described in the next section. The obtained solution is the values of the field variable at the grid points.

It is noted that the  $\theta$ -formulation (28) is the Euler explicit, fully implicit and semi-implicit (Crank-Nicolson) schemes for  $\theta = 0$ ,  $\theta = 1$  and  $\theta = 0.5$ , respectively.

**5.1.1 Semi-implicit scheme for temporal discretisation of the vorticity transport equation**

For 2-D planar flow problem, the Crank-Nicolson scheme is employed to discretise the vorticity transport equation (19) in the Cartesian coordinate system as follows.

$$\begin{aligned} \omega^{n+1} - \frac{\Delta t}{2Re} \left( \frac{\partial^2 \omega^{n+1}}{\partial x^2} + \frac{\partial^2 \omega^{n+1}}{\partial y^2} \right) &= \omega^n + \frac{\Delta t}{2Re} \left( \frac{\partial^2 \omega^n}{\partial x^2} + \frac{\partial^2 \omega^n}{\partial y^2} \right) \\ - \Delta t u^n \frac{\partial \omega^n}{\partial x} - \Delta t v^n \frac{\partial \omega^n}{\partial y} + \frac{\Delta t}{2Re} \left( \frac{\partial^2 (\tau_f^{xx})^n}{\partial x \partial y} + \frac{\partial^2 (\tau_f^{xy})^n}{\partial y^2} \right. \\ &\left. - \frac{\partial^2 (\tau_f^{yx})^n}{\partial x^2} - \frac{\partial^2 (\tau_f^{yy})^n}{\partial x \partial y} \right), \end{aligned} \quad (29)$$

where superscripts  $(n + 1)$ ,  $n$  and  $\Delta t$  are defined above. The components of fibre stress tensor  $\tau_f^{xx}$ ,  $\tau_f^{xy}$ ,  $\tau_f^{yx}$  and  $\tau_f^{yy}$  on the right-hand side (RHS) of Eq. (29) are known quantities, which are determined from the solution of the fibre configuration fields at the previous time step  $t^n$ .

For 2-D axisymmetric flow problems, the vorticity equation (24) is temporally discretised as follows.

$$\begin{aligned} \omega^{n+1} - \frac{\Delta t}{Re} \eta_a \left( \frac{\partial^2 \omega^{n+1}}{\partial z^2} + \frac{\partial^2 \omega^{n+1}}{\partial r^2} \right) &= \omega^n - \frac{\Delta t}{Re} (\eta_a - 1) \left( \frac{\partial^2 \omega^n}{\partial z^2} + \frac{\partial^2 \omega^n}{\partial r^2} \right) \\ + \frac{\Delta t}{Re} \left( \frac{1}{r} \frac{\partial \omega^n}{\partial r} - \frac{1}{r^2} \omega^n \right) - \Delta t u_z^n \frac{\partial \omega^n}{\partial z} - \Delta t u_r^n \frac{\partial \omega^n}{\partial r} + \Delta t \frac{u_r^n}{r} \omega^n \\ + \frac{\Delta t}{2Re} \left( \frac{\partial^2 (\tau_f^{rz})^n}{\partial r^2} - \frac{\partial^2 (\tau_f^{zr})^n}{\partial z^2} + \frac{\partial^2 (\tau_f^{zz})^n}{\partial r \partial z} - \frac{\partial^2 (\tau_f^{rr})^n}{\partial z \partial r} + \frac{1}{r} \frac{\partial (\tau_f^{rz})^n}{\partial r} \right. \\ &\left. - \frac{1}{r} \frac{\partial (\tau_f^{rr})^n}{\partial z} - \frac{1}{r^2} (\tau_f^{rz})^n \right), \end{aligned} \quad (30)$$

where the adaptive viscosity  $\eta_a$  is defined as before; and  $\tau_f^{zz}$ ,  $\tau_f^{zr}$ ,  $\tau_f^{rz}$  and  $\tau_f^{rr}$  are components of fibre stress tensor  $\boldsymbol{\tau}_f$ .

### 5.1.2 Euler explicit scheme for temporal discretisation of the equation of fibre configuration fields

As noted in section 2, the motion equation for fibres' direction (8) has been converted into the evolution equation (10) for the configuration  $\mathbf{Q}$  by executing a variable transformation in Eq. (9). Thus, the Euler explicit scheme is applied for Eq. (10) as follows.

$$\mathbf{Q}(\mathbf{x}, t^{n+1}) = \mathbf{Q}(\mathbf{x}, t^n) - \Delta t \mathbf{u}(\mathbf{x}, t^n) \cdot \nabla \mathbf{Q}(\mathbf{x}, t^n) + \Delta t (\nabla \mathbf{u}(\mathbf{x}, t^n))^T \cdot \mathbf{Q}(\mathbf{x}, t^n), \quad (31)$$

where  $t^n = n\Delta t$  and  $t^{n+1} = (n + 1)\Delta t$  are the times at steps  $n$  and  $(n + 1)$ , respectively;  $\Delta t$  the time step size for both micro and macro procedures as stated above.

In Eq. (31), the velocity field and its gradient are known and obtained from the macro procedure. Furthermore, in order to ensure the stability of the present method, the high-order upwind scheme (Ferreira, Tomé, Mangiacchi, Castelo, Cuminato, Fortuna, and McKee, 2002) is used to approximate the gradient of configuration fields ( $\nabla \mathbf{Q}$ ).

Since the configuration fields,  $\mathbf{Q}_i$ 's with  $i = (1, 2, \dots, N_f)$ , are independent from each other, Eq. (31) can be solved for each configuration field in parallel. The original fibre configuration fields  $\mathbf{P}_i$  are then calculated using Eq. (9). The fourth-order orientation tensor and the fibre stress are subsequently determined. Lastly, the gradient of the fibre stress tensor is approximated and introduced into the vorticity transport equation in the macro procedure.

**5.2 The 1D-IRBF based spatial discretisation scheme**

At a time  $t$ , the highest-order derivative of dependent variable  $\omega(x, t)$  (the second order in this work), the first order derivatives and the function itself are decomposed as follows [Mai-Duy, Le-Cao, and Tran-Cong (2008)].

$$\frac{d^2 \omega}{dx^2} = \sum_{j=1}^m w_j(t) g_j(x) = \sum_{j=1}^m w_j(t) G_j^{[2]}(x), \tag{32}$$

$$\frac{d \omega}{dx} = \sum_{j=1}^m w_j(t) G_j^{[1]}(x) + C_1(t), \tag{33}$$

$$\omega(x, t) = \sum_{j=1}^m w_j(t) G_j^{[0]}(x) + C_1(t)x + C_2(t), \tag{34}$$

where  $\{w_j(t)\}_{j=1}^m$  is the RBF weights;  $\{g_j(x)\}_{j=1}^m$  the RBFs;  $m$  a chosen number;  $G_j^{[1]}(x) = \int G_j^{[2]}(x) dx$ ;  $G_j^{[0]}(x) = \int G_j^{[1]}(x) dx$ ; and  $C_1$  and  $C_2$  are unknown integration constants at time  $t$ . In this paper, the multi-quadric RBF (MQ-RBF) is used and given by

$$g_j(x) = \sqrt{(x - c_j)^2 + a_j^2}, \tag{35}$$

where  $\{c_j\}_{j=1}^m$  and  $\{a_j\}_{j=1}^m$  are the RBF centres and widths, respectively. The centres are chosen to be the same as the data points  $x_j$  in this work.

Eqs. (32), (33) and (34) are evaluated at every collocation point and re-arranged to

produce the following set of algebraic equations

$$\frac{d^2 \widehat{\boldsymbol{\omega}}}{dx^2} = \widehat{\mathbf{G}}^{[2]}(x) \widehat{\mathbf{w}}(t), \tag{36}$$

$$\frac{d \widehat{\boldsymbol{\omega}}}{dx} = \widehat{\mathbf{G}}^{[1]}(x) \widehat{\mathbf{w}}(t), \tag{37}$$

$$\widehat{\boldsymbol{\omega}} = \widehat{\mathbf{G}}^{[0]}(x) \widehat{\mathbf{w}}(t), \tag{38}$$

where

$$\widehat{\mathbf{w}} = ( w_1(t) \quad w_2(t) \quad \cdots \quad w_m(t) \quad C_1(t) \quad C_2(t) )^T;$$

$$\widehat{\boldsymbol{\omega}} = ( \omega_1(t) \quad \omega_2(t) \quad \cdots \quad \omega_m(t) )^T \text{ with } \omega_j = \omega(x_j);$$

$$\frac{d^k \widehat{\boldsymbol{\omega}}}{dx^k} = \left( \frac{d^k \omega_1(x,t)}{dx^k} \quad \frac{d^k \omega_2(x,t)}{dx^k} \quad \cdots \quad \frac{d^k \omega_m(x,t)}{dx^k} \right)^T \text{ with } k = \{1,2\};$$

$$\widehat{\mathbf{G}}^{[2]} = \begin{bmatrix} G_1^{[2]}(x_1) & \cdots & G_m^{[2]}(x_1) & 0 & 0 \\ G_1^{[2]}(x_2) & \cdots & G_m^{[2]}(x_2) & 0 & 0 \\ \vdots & \ddots & \vdots & \vdots & \vdots \\ G_1^{[2]}(x_m) & \cdots & G_m^{[2]}(x_m) & 0 & 0 \end{bmatrix};$$

$$\widehat{\mathbf{G}}^{[1]} = \begin{bmatrix} G_1^{[1]}(x_1) & \cdots & G_m^{[1]}(x_1) & 1 & 0 \\ G_1^{[1]}(x_2) & \cdots & G_m^{[1]}(x_2) & 1 & 0 \\ \vdots & \ddots & \vdots & \vdots & \vdots \\ G_1^{[1]}(x_m) & \cdots & G_m^{[1]}(x_m) & 1 & 0 \end{bmatrix}; \text{ and}$$

$$\widehat{\mathbf{G}}^{[0]} = \begin{bmatrix} G_1^{[0]}(x_1) & \cdots & G_m^{[0]}(x_1) & x_1 & 1 \\ G_1^{[0]}(x_2) & \cdots & G_m^{[0]}(x_2) & x_2 & 1 \\ \vdots & \ddots & \vdots & \vdots & \vdots \\ G_1^{[0]}(x_m) & \cdots & G_m^{[0]}(x_m) & x_m & 1 \end{bmatrix}.$$

Owing to the presence of integration constants, more additional constraints can be incorporated into the algebraic equation system through Eq. (38) as follows.

$$\begin{pmatrix} \widehat{\boldsymbol{\omega}} \\ \widehat{\mathbf{f}} \end{pmatrix} = \widehat{\mathbf{C}} \widehat{\mathbf{w}},$$

where  $\widehat{\mathbf{C}} = \begin{bmatrix} \widehat{\mathbf{G}}^{[0]} \\ \widehat{\mathbf{L}} \end{bmatrix}$ ; and  $\widehat{\mathbf{f}} = \widehat{\mathbf{L}} \widehat{\mathbf{w}}$  are additional constraints. The conversion of the

network-weight space into the physical space yields

$$\widehat{\mathbf{w}} = \widehat{\mathbf{C}}^{-1} \begin{pmatrix} \widehat{\boldsymbol{\omega}} \\ \widehat{\mathbf{f}} \end{pmatrix}, \tag{39}$$

where  $\widehat{\mathbf{C}}^{-1}$  is the conversion matrix. Eq. (39) is substituted into Eqs. (32) and (33) to obtain the second and first-order derivatives of  $\omega$  in terms of nodal variable values as follows.

$$\frac{d^2\omega}{dx^2} = \mathcal{D}_2\widehat{\boldsymbol{\omega}} + k_2, \quad \frac{d\omega}{dx} = \mathcal{D}_1\widehat{\boldsymbol{\omega}} + k_1 \tag{40}$$

where  $\mathcal{D}_1$  and  $\mathcal{D}_2$  are known vectors of length  $m$ ; and  $k_2$  and  $k_1$  are scalars determined by  $\widehat{\mathbf{f}}$ . Applying Eq. (40) at every collocation point on the grid lines yields

$$\frac{d^2\widehat{\boldsymbol{\omega}}}{dx^2} = \widehat{\mathcal{D}}_{2x}\widehat{\boldsymbol{\omega}} + \widehat{\mathbf{k}}_{2x}, \quad \frac{d\widehat{\boldsymbol{\omega}}}{dx} = \widehat{\mathcal{D}}_{1x}\widehat{\boldsymbol{\omega}} + \widehat{\mathbf{k}}_{1x} \tag{41}$$

where  $\widehat{\mathcal{D}}_{2x}$  and  $\widehat{\mathcal{D}}_{1x}$  are known matrices of dimension  $m \times m$ ; and  $\widehat{\mathbf{k}}_{2x}$  and  $\widehat{\mathbf{k}}_{1x}$  are known vectors of length  $m$ ;  $m$  is defined as before. The subscript  $x$  expresses the spatial direction, in which the matrices  $\widehat{\mathcal{D}}_{2x}$ ,  $\widehat{\mathcal{D}}_{1x}$  and the vectors  $\widehat{\mathbf{k}}_{2x}$ ,  $\widehat{\mathbf{k}}_{1x}$  are constructed. For two-dimensional problems, a similar process is carried out in the  $y$ -direction in order to achieve known matrices and vectors  $\widehat{\mathcal{D}}_{2y}$ ,  $\widehat{\mathcal{D}}_{1y}$ ,  $\widehat{\mathbf{k}}_{2y}$  and  $\widehat{\mathbf{k}}_{1y}$ . The algorithm of the present multiscale method is detailed in the next section.

## 6 Algorithm of the present method

The algorithm of the present method is presented in this section. The implementation will be then described in several illustrative examples in the next section.

- (a) Generate a set of collocation points on the considered domain. The initial and boundary conditions of the velocity field and fibre configurations are correspondingly assigned at each collocation point. The stream function's and vorticity's initial and boundary conditions are then determined using Eqs. (16), (17) and (18) for planar flow problems or Eqs. (20), (21) and (23) for axisymmetric ones. Meanwhile, the initial fibre configurations including a set of randomly oriented unit vectors  $\mathbf{P}$ 's and the transformed vectors  $\mathbf{Q}$ 's are defined by Eq. (9);
- (b) Assign  $N_f$  fibres to each collocation point based on the BCF idea. All fibres having the same index constitute a fibre configuration field. Hence, there is an ensemble of  $N_f$  fibre configuration fields;

- (c) Velocity gradients and the strain rate tensor  $\mathbf{D}$  are directly calculated from the current velocity field.
- (d) Solve the evolution equation of fibres (31) for the new configurations ( $\mathbf{Q}$ 's). Determine the orientation vectors of fibre configurations using Eq. (9) and then calculate the fourth-order orientation tensor  $\langle \mathbf{PPPP} \rangle$  and the fibre stress tensor at each collocation point. The gradients of fibre stresses are calculated in advance and will be used in the following step as known quantities in the vorticity transport equation;
- (e) Solve the stream function equation for the new solution and then calculate the new velocity field. The new velocity field together with the gradients of the fibre stress components obtained by step (d) are used to solve the vorticity equation;
- (f) Terminate the simulation when either the desired time or convergence is reached. The latter is determined by a convergence measure ( $CM$ ) for the velocity, defined by

$$CM(\mathbf{u}) = \sqrt{\frac{\sum_1^N \sum_{i=1}^{d_s} (u_i^n - u_i^{n-1})^2}{\sum_1^N \sum_{i=1}^{d_s} (u_i^n)^2}} \leq tol \quad (42)$$

where  $d_s$  is the number of dimensions;  $tol$  a preset tolerance;  $u_i$  the  $i$ -component of the velocity at a collocation point;  $N$  the number of collocation points and  $n$  the iteration number.

- (g) Return to step (c) for the next time step until the steady state or a given time is reached.

## 7 Numerical examples

The present method is employed to simulate fibre suspension flows between two parallel plates (a planar channel) and through a circular tube. The capability of the present method is then demonstrated with the simulation of the axisymmetric contraction flow of fibre suspension. The obtained results of the first problem are compared with the results published by Chiba, Yasuda, and Nakamura (2001) whereas the solutions to the last problem are compared with those presented in Chiba, Nakamura, and Boger (1990) and Lipscomb, Denn, Hur, and Boger (1988). In order to compare the present results with those cited above, we also choose  $\lambda = 1$ , and as a result  $\zeta = 0$  in Eq. (10) as shown in the examples below.

7.1 Fibre suspension flow between two parallel plates

This problem was studied by Chiba, Yasuda, and Nakamura (2001). The geometry of the problem is given in Fig. 1 where  $L = 10$  and  $H = 1$  are the length and height of the channel, respectively.

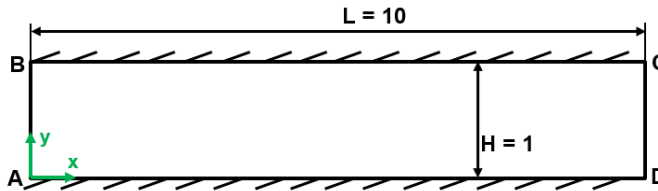


Figure 1: Flow through two parallel plates: the geometry of the problem.

7.1.1 Governing equations and boundary conditions

The system of governing equations for this particular problem is obtained from the discussion in sections 2 and 4 as follows.

$$\frac{\partial \omega}{\partial t} + u \frac{\partial \omega}{\partial x} + v \frac{\partial \omega}{\partial y} = \frac{1}{\text{Re}} \left( \frac{\partial^2 \omega}{\partial x^2} + \frac{\partial^2 \omega}{\partial y^2} \right) + \frac{1}{2\text{Re}} \left( \frac{\partial^2 \tau_f^{xx}}{\partial x \partial y} + \frac{\partial^2 \tau_f^{xy}}{\partial y^2} - \frac{\partial^2 \tau_f^{yx}}{\partial x^2} - \frac{\partial^2 \tau_f^{yy}}{\partial x \partial y} \right), \tag{43}$$

$$\frac{\partial^2 \Psi}{\partial x^2} + \frac{\partial^2 \Psi}{\partial y^2} = 2\omega, \tag{44}$$

$$u = \frac{\partial \Psi}{\partial y}, \quad v = -\frac{\partial \Psi}{\partial x}, \tag{45}$$

$$\frac{\partial \mathbf{Q}}{\partial t} + \mathbf{u} \cdot \nabla \mathbf{Q} = (\nabla \mathbf{u})^T \cdot \mathbf{Q}, \tag{46}$$

$$\langle \mathbf{P} \mathbf{P} \mathbf{P} \mathbf{P} \rangle = \left\langle \frac{\mathbf{Q} \mathbf{Q} \mathbf{Q} \mathbf{Q}}{\mathcal{Q} \mathcal{Q} \mathcal{Q} \mathcal{Q}} \right\rangle, \tag{47}$$

$$\boldsymbol{\tau}_f = k_f \mathbf{D} : \langle \mathbf{P} \mathbf{P} \mathbf{P} \mathbf{P} \rangle. \tag{48}$$

In the system of equations (43) - (48), the first three equations relate to solutions of stream function, vorticity and velocity variables of the flow, while the next two equations are for solutions of the fibre configuration fields  $\mathbf{Q}$ 's and  $\mathbf{P}$ 's. The solutions at two different scales are linked together by the last equation, which is to calculate the fibre stress tensor  $\boldsymbol{\tau}_f$ .

Boundary conditions are applied to the problem as follows.

- At the inlet  $\overline{AB}$ :
  - A parabolic velocity profile of the Newtonian fluid is applied, i.e.  $u = u_{max} \left( 1 - \left( \frac{2y}{H} - 1 \right)^2 \right)$  and  $v = 0$ , where  $u_{max} = 1.5$  is the maximum value of the velocity profile;
  - For the fibre configuration field, a set of  $N_f$  fibres are generated and assigned at each collocation point on the inlet boundary. A fibre  $i$  is defined by its angle  $\theta_i = -\frac{\pi}{2} + \frac{\pi(i-1)}{N_f}$ , ( $i = 1, \dots, N_f$ );
- On the walls  $\overline{BC}$  and  $\overline{AD}$ :
  - There is no-slip boundary condition for the velocity field, i.e.  $u = 0$  and  $v = 0$ ;
  - The condition of co-linear alignment is used for the fibre configuration fields, i.e.  $\theta_i = 0$ ;
- At the outlet  $\overline{DC}$ : The flow out condition is applied, i.e.  $\frac{\partial u}{\partial x} = 0$  and  $v = 0$ .

### 7.1.2 Discretisation of governing equations and numerical results

Applying the temporal discretisation schemes presented in section 5 to the vorticity transport equation and the evolution equation of fibre configurations in 2-dimensional space yields the following equations

$$\omega^{n+1} - \frac{\Delta t}{2Re} \left( \frac{\partial^2 \omega^{n+1}}{\partial x^2} + \frac{\partial^2 \omega^{n+1}}{\partial y^2} \right) = \omega^n + \frac{\Delta t}{2Re} \left( \frac{\partial^2 \omega^n}{\partial x^2} + \frac{\partial^2 \omega^n}{\partial y^2} \right) - \Delta t u^n \cdot \frac{\partial \omega^n}{\partial x} - \Delta t v^n \frac{\partial \omega^n}{\partial y} + \frac{\Delta t}{2Re} \left( \frac{\partial^2 (\tau_f^{xx})^n}{\partial x \partial y} + \frac{\partial^2 (\tau_f^{xy})^n}{\partial y^2} - \frac{\partial^2 (\tau_f^{yx})^n}{\partial x^2} - \frac{\partial^2 (\tau_f^{yy})^n}{\partial x \partial y} \right), \quad (49)$$

$$Q_x^{n+1} = Q_x^n - \Delta t \left( u^n \frac{\partial Q_x^n}{\partial x} + v^n \frac{\partial Q_x^n}{\partial y} \right) + \Delta t \left( \frac{\partial u^n}{\partial x} Q_x^n + \frac{\partial u^n}{\partial y} Q_y^n \right), \quad (50)$$

$$Q_y^{n+1} = Q_y^n - \Delta t \left( u^n \frac{\partial Q_y^n}{\partial x} + v^n \frac{\partial Q_y^n}{\partial y} \right) + \Delta t \left( \frac{\partial v^n}{\partial x} Q_x^n + \frac{\partial v^n}{\partial y} Q_y^n \right), \quad (51)$$

where superscripts  $n$  and  $(n+1)$  indicate the two successive time steps  $t_n = n\Delta t$  and  $t_{n+1} = (n+1)\Delta t$ ;  $Q_x^{n+1}$  and  $Q_y^{n+1}$  the two components of vector  $\mathbf{Q}$  along  $x$  and  $y$

directions at the time  $t_{n+1}$ , respectively. The time step size is chosen  $\Delta t = 0.001$ . A range of fibre parameters,  $k_f = \{2, 4, 6, 8, 10, 12\}$  is considered. Other parameters of the fluid include the Reynolds number,  $Re = 10$  and the number of configuration fields,  $N_f = 180$ .

A grid convergence study for the flow with  $k_f = 12$  is done with four different uniform Cartesian grids, whose grid parameters are given in Table 1. The four grids are labelled as M1, M2, M3 and M4 where M1 is the coarsest one and M4 is the finest one.

Table 1: A grid convergence study for the fibre suspension flow between two parallel plates. Four different grids are used where  $\Delta x$  and  $\Delta y$  are grid spaces in  $x$ -direction and  $y$ -direction, respectively; and  $N_x$  and  $N_y$  the number of grid nodes in each direction.

Grid's label	$\Delta x$	$\Delta y$	$N_x \times N_y$
M1	1/16	1/16	161 $\times$ 17
M2	1/18	1/18	181 $\times$ 19
M3	1/20	1/20	201 $\times$ 21
M4	1/24	1/24	241 $\times$ 25

The convergence of the solutions with four different meshes is confirmed through the convergence measure of the velocity field introduced in Fig. 2. Meanwhile, the grid convergence is reflected through the centreline velocity profile and the distribution of the extra shear stress at the outlet in Fig. 3.

Grid M3, with  $\Delta x = \Delta y = 0.05$  presented in Fig. 4, is chosen for all simulation cases in this problem. The numerical results obtained by the present method confirm a very good agreement with those by Chiba, Yasuda, and Nakamura (2001) using the finite difference method and the statistical scheme and a much finer mesh of  $\Delta x = \Delta y = 0.025$ . Several observations are presented as follows.

The orientation of fibres at a position in the flow is illustrated by the ellipse's geometry (Fig. 5) whose length and direction of two axes are determined by the eigenvalues and the eigenvectors of the second-order orientation tensor  $\langle \mathbf{PP} \rangle$ . Thus, there are three cases: a) a circle/circular ellipse indicates an isotropic orientation of fibres at a position; b) an ellipse implies that the predominant direction of fibres is parallel with its major axis and c) a straight line depicts that all fibres completely align with the line.

Fig. 6 shows that the fibres near the channel wall tend to align with the flow direction ( $x$ ) whereas the fibres' orientation is isotropic at the centreline. The relationship between the shear stress and the fibre's orientation will be discussed later in

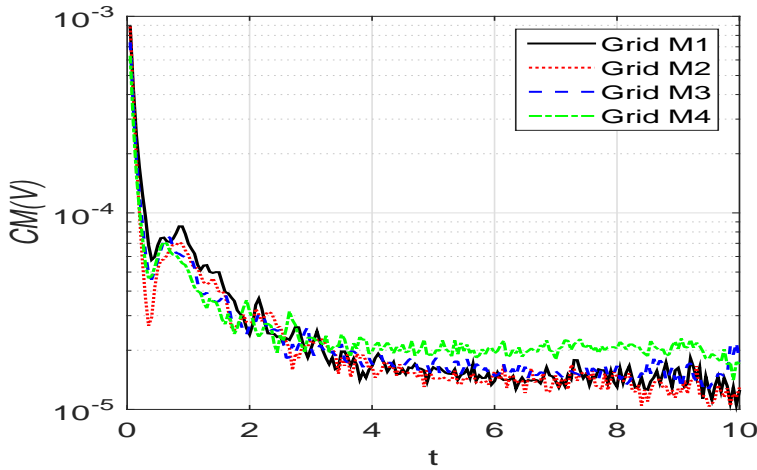


Figure 2: A grid convergence study for flow with  $k_f = 12$ : the convergence measure of the velocity field for grids M1, M2, M3, and M4.

this section. The results in Fig. 6 whose top figure is for  $k_f = 2$  and bottom one for  $k_f = 10$  also show that the fibre parameter does not significantly affect the fibres' orientation in the flow.

Furthermore, Fig. 7 presents the distribution of the components  $P_{1111}$  (top figure) and  $P_{1122}$  (bottom figure) of the fourth-order tensor  $\langle \mathbf{PPPP} \rangle$  on several vertical planes ( $x_i = \{0.05, 0.15, 0.25, 0.5, 0.75, 1, 1.25, 2.5, 5, 7.5, 10\}$ ) along the channel's length with respect to  $y$  (across the channel). The results show that more and more fibres tend to align with the main flow direction ( $x$ ) as they approach the outlet, especially in the near-wall region.

Fig. 8 depicts the development of velocity along the centreline of the channel with a range of fibre parameters  $k_f = \{2, 4, 6, 8, 10, 12\}$ . The undershoot is observed in all cases and the undershoot is more pronounced as the fibre parameter increases. The undershoot reflects the effect of the isotropy of fibre configurations at the inlet. The isotropy of fibre configurations resists the development of velocity ( $u$ ) on the flow direction ( $x$ ) at the region near the inlet. The velocity then increases along the flow direction to the outlet with a gradual decrease of the isotropy of fibres orientation as described in Fig. 6.

Numerical experiments show that the fibre parameter has a considerable effect on the transient velocity field near the inlet (Fig. 8). In the downstream direction, as the flow becomes more and more developed, there is insignificant difference between the velocity profiles at the outlet as shown in Fig. 9.

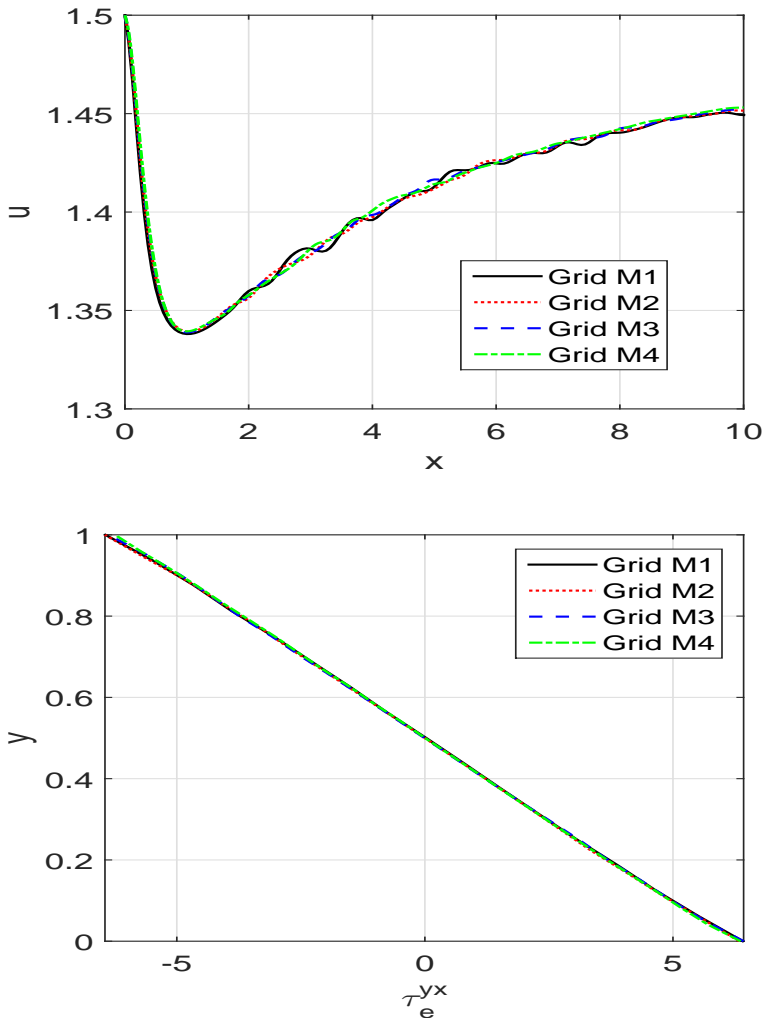


Figure 3: A grid convergence study for flow with  $k_f = 12$ : the axial velocity distribution on the centreline (top figure) and the distribution of the extra shear stress at the outlet (bottom figure) for grids M1, M2, M3, and M4.

Finally, the distributions of the shear stress ( $T_{xy}$ ) and the first normal stress difference ( $T_{xx} - T_{yy}$ ) for the flow with  $k_f = 10$  are presented in Fig. 10. In contrast to the Newtonian flow, a high-stress concentration for the shear stress (left figure) and the first normal stress difference (right figure) appears near the corner between the inlet and the walls in the fibre suspension flow. The reason of the high-stress con-

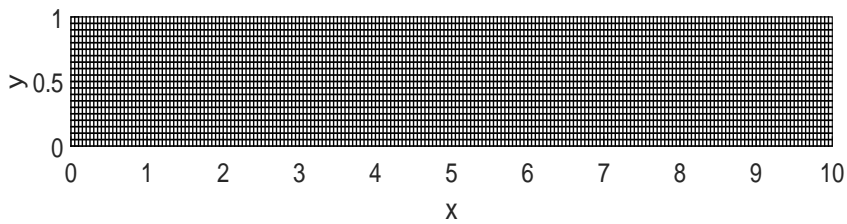


Figure 4: Flow through two parallel plates: a uniform Cartesian grid.

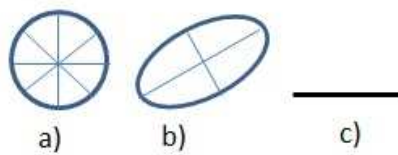


Figure 5: Orientation of fibres: a) Circle: the fibres' direction is isotropic; b) Ellipse: the major axis is the predominant direction of fibres and c) Straight line: all fibres completely align with the line.

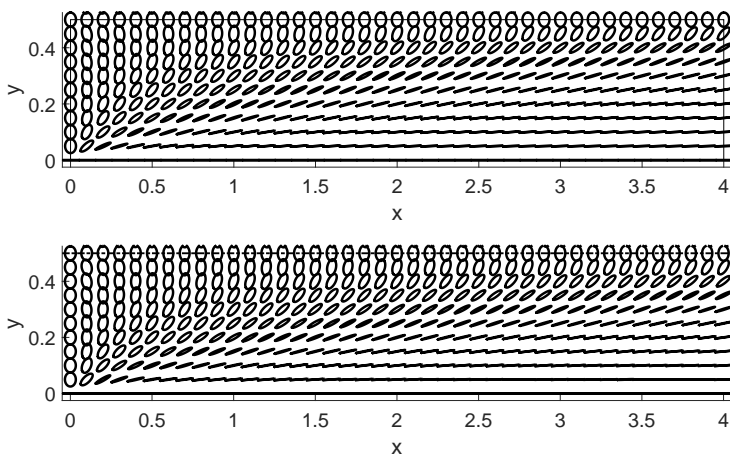


Figure 6: Fibre suspension flow between two parallel plates: the evolution of fibres' orientation along the channel with  $k_f = 2$  (top figure) and  $k_f = 10$  (bottom figure).

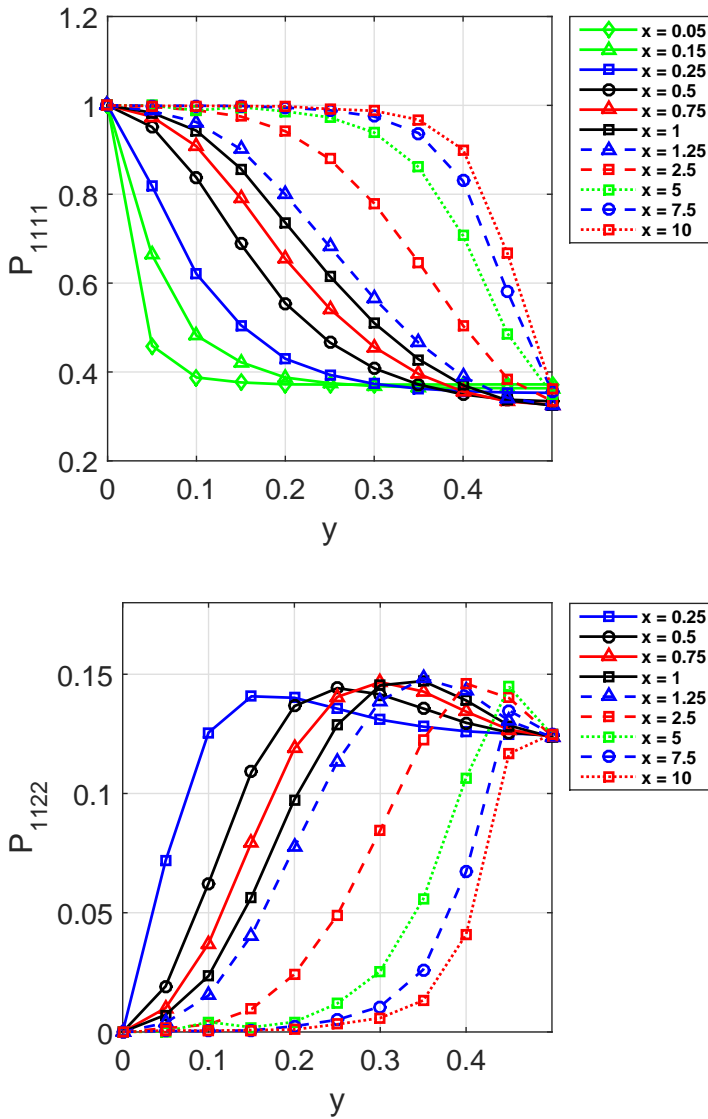


Figure 7: Fibre suspension flow between two parallel plates: the distribution of components  $P_{1111}$  (top figure) and  $P_{1122}$  (bottom figure) of the fourth-order orientation tensor on several vertical planes ( $\{x_i = 0.05, 0.15, 0.25, 0.5, 0.75, 1, 1.25, 2.5, 5, 7.5, 10\}$ ) with respect to  $y$  using  $k_f = 10$ .

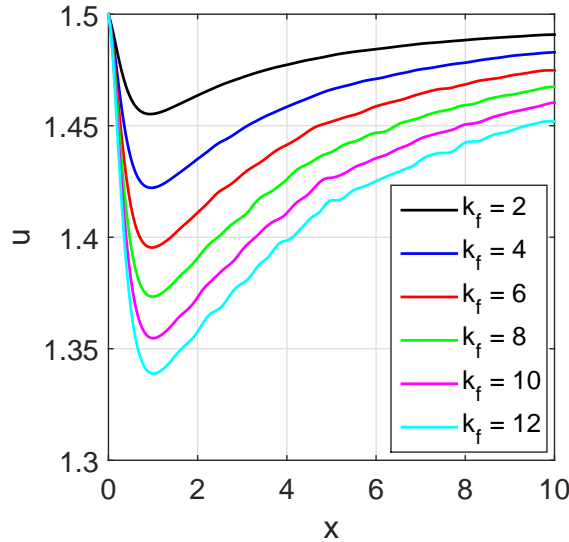


Figure 8: Fibre suspension flow between two parallel plates: the centreline velocity profiles for flows with  $k_f = \{2, 4, 6, 8, 10, 12\}$ .

centration is the anisotropy of fibres' orientation near the corner (see Fig. 6), where there is a steep transition between two extreme states of fibres' orientation, namely the co-linear alignment configuration on the wall and the isotropic configuration at the inlet. The distribution of  $T_{xy}$  and  $T_{xx} - T_{yy}$  together with their values are in very good agreement with those presented in Chiba, Yasuda, and Nakamura (2001).

On the efficiency of the present method, the convergence measures ( $CM$ 's) of the vorticity, stream function and velocity fields are presented in Fig. 11, where the top figure is for  $k_f = 2$  and the bottom figure for  $k_f = 10$ . The convergence in the present method is significantly improved in comparison with one achieved by Chiba, Yasuda, and Nakamura (2001). Specifically, with  $k_f = 10$  the present method achieves a convergence measure of approximately  $3E-4$  for vorticity and  $2E-6$  for stream function (Fig. 11 - bottom figure) using a much coarser mesh (a factor of 2 in each of the coordinate directions). Furthermore, the results depict that  $CM$ s decrease with increasing value of the fibre parameter, for example,  $CM(\omega) \approx 3E-5$ ,  $CM(\Psi) \approx 2E-7$ ,  $CM(V) \approx 1E-6$  for  $k_f = 2$  and  $CM(\omega) \approx 3E-4$ ,  $CM(\Psi) \approx 2E-6$ ,  $CM(V) \approx 1E-5$  for  $k_f = 10$ . Finally, the efficiency of the present method can also be improved by increasing the number of fibre configuration fields (see Fig. 12).

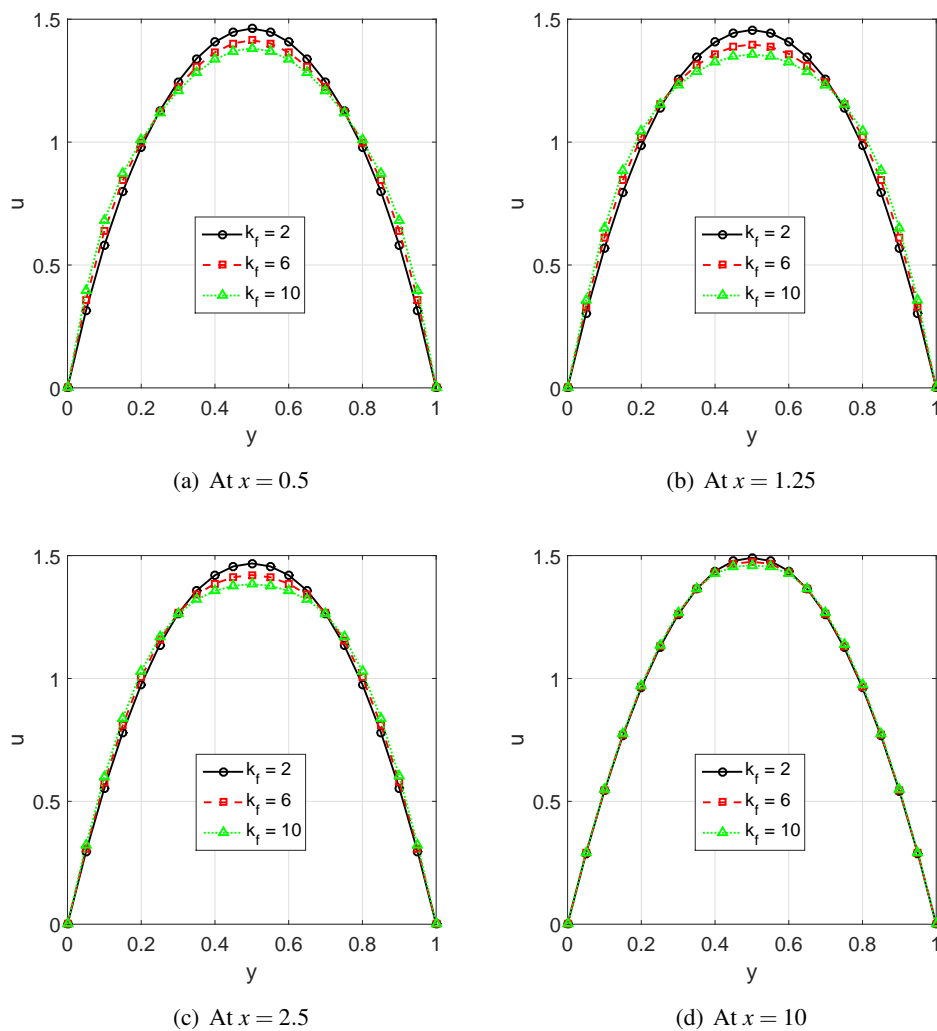


Figure 9: Fibre suspension flow between two parallel plates: the effect of the fibre parameter  $k_f$  on the axial velocity profiles at several sections  $x = \{0.5, 1.25, 2.5, 10\}$  of the channel.

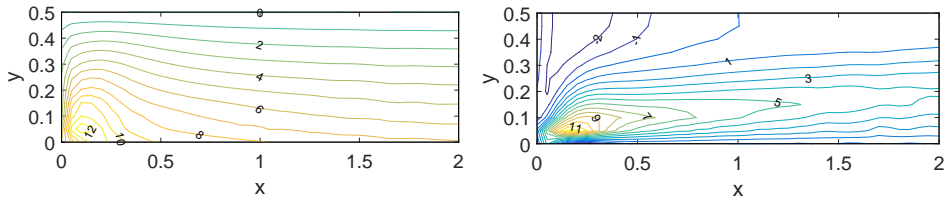


Figure 10: Fibre suspension flow between two parallel plates: the distribution of shear stress (left figure) and the first normal stress difference (right figure) in the fibre suspension flow with  $k_f = 10$ .

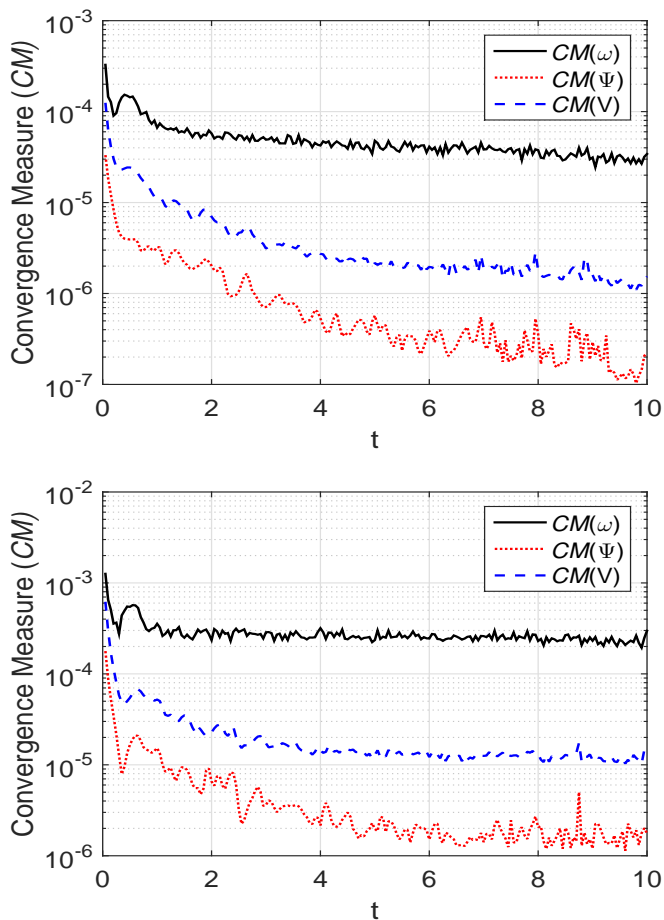


Figure 11: Fibre suspension flow between two parallel plates: the convergence measure for vorticity, stream function and velocity fields of flows with  $k_f = 2$  (top figure) and  $k_f = 10$  (bottom figure).

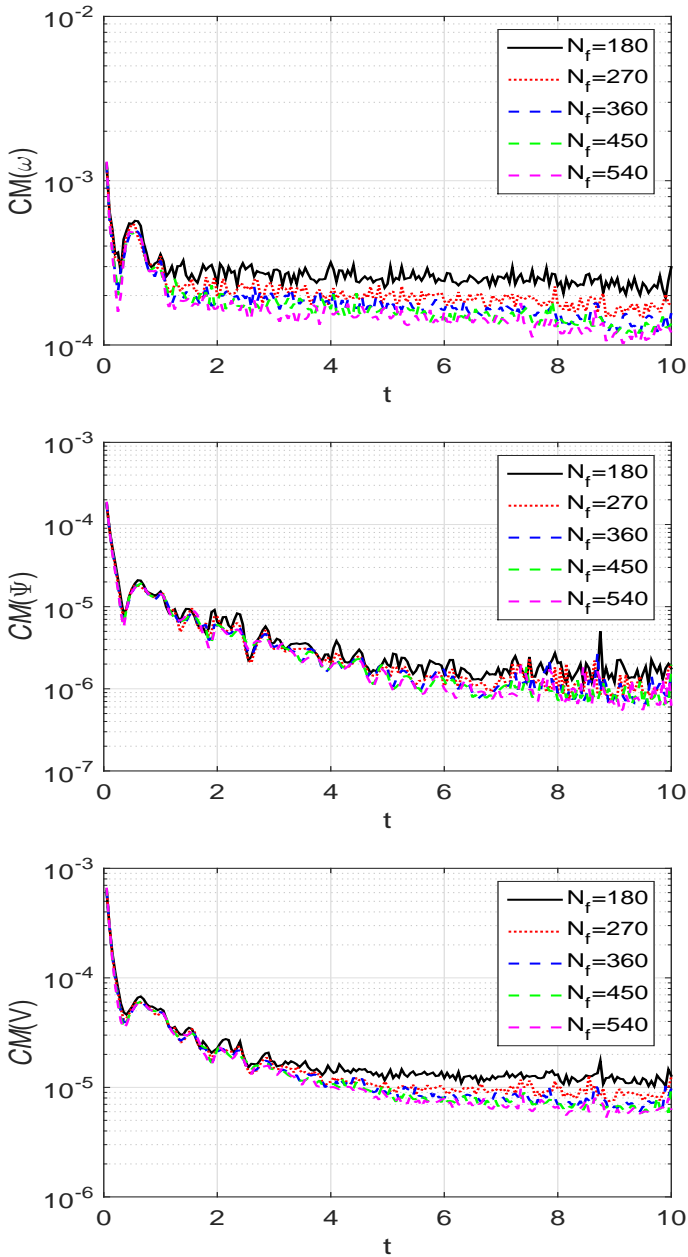


Figure 12: Fibre suspension flow between two parallel plates: the convergence measure for vorticity (top figure), stream function (middle figure) and velocity field (bottom figure) of flows using several fibre configuration fields  $N_f = \{180, 270, 360, 450, 540\}$ .

### 7.2 Fibre suspension flow through a circular tube

This problem is simulated using the same parameters as described in the fibre suspension flow between two parallel plates. The obtained results are compared with those for fibre suspension flow between two parallel plates. Furthermore, the velocity profile as well as the vorticity and stream function at the outlet will be used to determine several Dirichlet boundary conditions for the fibre suspension flow through an axisymmetric contraction presented in section 7.3.

The flow through a circular tube is described in Fig. 13 where a half of the flow’s domain is considered, owing to the geometrical symmetry. For this problem,  $L = 10$  is the length of the tube and  $R = 0.5$  the tube’s radius. The other parameters include the Reynolds number  $Re = 10$ , time step size  $\Delta t = 1E-3$  and the number of fibre configuration fields  $N_f = 180$ .

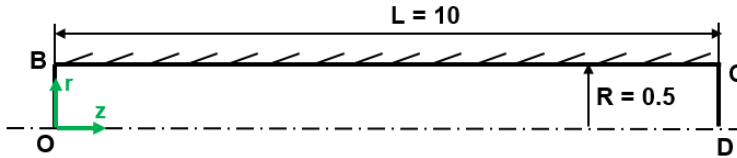


Figure 13: Fibre suspension flow through a circular tube: the geometry of the problem.

#### 7.2.1 Governing equations and boundary conditions

The governing equations for this particular problem is obtained from sections 2 and 4 as follows.

$$\begin{aligned} \frac{\partial \omega}{\partial t} + u_z \frac{\partial \omega}{\partial z} + u_r \frac{\partial \omega}{\partial r} - \frac{u_r}{r} \omega - \frac{1}{Re} \eta_a \left( \frac{\partial^2 \omega}{\partial z^2} + \frac{\partial^2 \omega}{\partial r^2} \right) = \\ - \frac{1}{Re} (\eta_a - 1) \left( \frac{\partial^2 \omega}{\partial z^2} + \frac{\partial^2 \omega}{\partial r^2} \right) + \frac{1}{Re} \left( \frac{1}{r} \frac{\partial \omega}{\partial r} - \frac{1}{r^2} \omega \right) + \\ \frac{1}{2Re} \left( \frac{\partial^2 \tau_f^{rz}}{\partial r^2} - \frac{\partial^2 \tau_f^{rz}}{\partial z^2} + \frac{\partial^2 \tau_f^{zz}}{\partial r \partial z} - \frac{\partial^2 \tau_f^{rr}}{\partial z \partial r} + \frac{1}{r} \frac{\partial \tau_f^{rz}}{\partial r} - \frac{1}{r} \frac{\partial \tau_f^{rr}}{\partial z} - \frac{1}{r^2} \tau_f^{rz} \right), \end{aligned} \tag{52}$$

$$\frac{1}{r} \frac{\partial^2 \Psi}{\partial z^2} + \frac{1}{r} \frac{\partial^2 \Psi}{\partial r^2} - \frac{1}{r^2} \frac{\partial \Psi}{\partial r} = 2\omega, \tag{53}$$

$$u_z = \frac{1}{r} \frac{\partial \Psi}{\partial r}, \quad u_r = -\frac{1}{r} \frac{\partial \Psi}{\partial z}, \tag{54}$$

$$\frac{\partial \mathbf{Q}}{\partial t} + \mathbf{u} \cdot \nabla \mathbf{Q} = (\nabla \mathbf{u})^T \cdot \mathbf{Q}, \quad (55)$$

$$\langle \mathbf{PPPP} \rangle = \left\langle \frac{\mathbf{Q} \mathbf{Q} \mathbf{Q} \mathbf{Q}}{\underline{Q} \underline{Q} \underline{Q} \underline{Q}} \right\rangle, \quad (56)$$

$$\boldsymbol{\tau}_f = k_f \mathbf{D} : \langle \mathbf{PPPP} \rangle, \quad (57)$$

where the parameters in the system (52) - (57) were presented before. For the numerical stability of the present method, the vorticity transport equation (52) is developed using the DAVSS scheme as follows.

$$\begin{aligned} \omega^{n+1} - \frac{\Delta t}{Re} \eta_a \left( \frac{\partial^2 \omega^{n+1}}{\partial z^2} + \frac{\partial^2 \omega^{n+1}}{\partial r^2} \right) &= \omega^n - \frac{\Delta t}{Re} (\eta_a - 1) \left( \frac{\partial^2 \omega^n}{\partial z^2} + \frac{\partial^2 \omega^n}{\partial r^2} \right) \\ + \frac{\Delta t}{Re} \left( \frac{1}{r} \frac{\partial \omega^n}{\partial r} - \frac{1}{r^2} \omega^n \right) - \Delta t u_z^n \frac{\partial \omega^n}{\partial z} - \Delta t u_r^n \frac{\partial \omega^n}{\partial r} + \Delta t \frac{u_r^n}{r} \omega^n \\ + \frac{\Delta t}{2Re} \left( \frac{\partial^2 (\tau_f^{rz})^n}{\partial r^2} - \frac{\partial^2 (\tau_f^{rz})^n}{\partial z^2} + \frac{\partial^2 (\tau_f^{zz})^n}{\partial r \partial z} - \frac{\partial^2 (\tau_f^{rr})^n}{\partial z \partial r} + \frac{1}{r} \frac{\partial (\tau_f^{rz})^n}{\partial r} \right. \\ \left. - \frac{1}{r} \frac{\partial (\tau_f^{rr})^n}{\partial z} - \frac{1}{r^2} (\tau_f^{rz})^n \right), \end{aligned} \quad (58)$$

Similar to the previous problem, the boundary conditions are given by

- At the inlet  $\overline{OB}$ :
  - A Newtonian parabolic velocity profile is applied, i.e.  $u_z = u_{max} \left( 1 - \left( \frac{r}{R} \right)^2 \right)$  and  $u_r = 0$ , where  $u_{max} = 1.5$  is the maximum value of the velocity profile;
  - For the fibre configuration field, a set of  $N_f = 180$  fibres are generated and assigned at each collocation point on the inlet boundary. A fibre  $i$  is defined by the angle  $\theta_i = -\frac{\pi}{2} + \frac{\pi(i-1)}{N_f}$ , ( $i = 1, \dots, N_f$ );
- On the wall  $\overline{BC}$ :
  - No-slip boundary condition is used, i.e.  $u_z = 0$  and  $u_r = 0$ ;

- For the fibre configuration, the co-linear alignment condition is imposed on the wall, i.e.  $\theta_i = 0$ ;
- At the outlet  $\overline{DC}$ : A flow out condition is used, i.e.  $\frac{\partial u_z}{\partial z} = 0$  and  $u_r = 0$ ;
- On the centreline  $\overline{OD}$ : The symmetric boundary condition is imposed, i.e.  $\frac{\partial u_z}{\partial r} = 0$  and  $u_r = 0$ .

### 7.2.2 Discretisation of governing equations

The temporal discretisation of the fibre configuration field  $\mathbf{Q}$  is described in the axisymmetric cylindrical coordinates as follows.

$$Q_z^{n+1} = Q_z^n - \Delta t \left( u_z^n \frac{\partial Q_z^n}{\partial z} + u_r^n \frac{\partial Q_z^n}{\partial r} \right) + \Delta t \left( \frac{\partial u_z^n}{\partial z} Q_z^n + \frac{\partial u_r^n}{\partial r} Q_r^n \right), \tag{59}$$

$$Q_r^{n+1} = Q_r^n - \Delta t \left( u_z^n \frac{\partial Q_r^n}{\partial z} + u_r^n \frac{\partial Q_r^n}{\partial r} \right) + \Delta t \left( \frac{\partial u_r^n}{\partial z} Q_z^n + \frac{\partial u_r^n}{\partial r} Q_r^n \right), \tag{60}$$

where parameters were defined before. A non-uniform grid described in Fig. 14 is installed for the simulation with  $\Delta z_1 = 0.05, \forall z \in [0, 9.9]$  and  $\Delta z_2 = 0.01, \forall z \in [9.9, 10]$ ;  $\Delta r_1 = 0.01, \forall r \in [0, 0.1]$ ; and  $\Delta r_2 = 0.05, \forall r \in [0.1, 0.5]$ . Experiences show that finer meshes near the outlet and the centreline are necessary for an accurate solution at these regions.

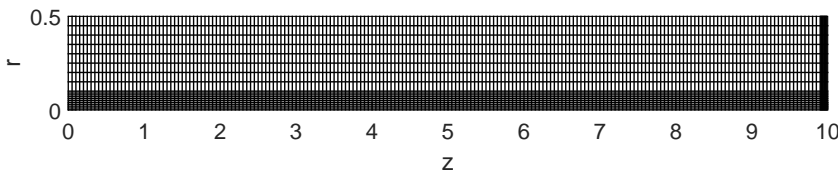


Figure 14: Fibre suspension flow through a circular tube: a non-uniform Cartesian grid for the problem.

### 7.2.3 Results and discussion

Fig. 15 depicts the velocity distribution of fibre suspension flows along the centreline of the tube for a range of fibre parameters  $k_f = \{2, 6, 10\}$ . An undershoot is also observed in all cases of fibre parameter (solid lines) as in the flow between two parallel plates (dashed lines) but much stronger. Furthermore, the undershoot's positions are closer to the entrance than the ones in the flows between two parallel plates. The undershoot's feature is presented in detail in Table 2 for the fibre

suspension flows between two parallel plates and a circular tube. The influence of the fibre parameter on the undershoot feature of velocity profiles for both fibre suspension flows is illustrated in Fig. 16.

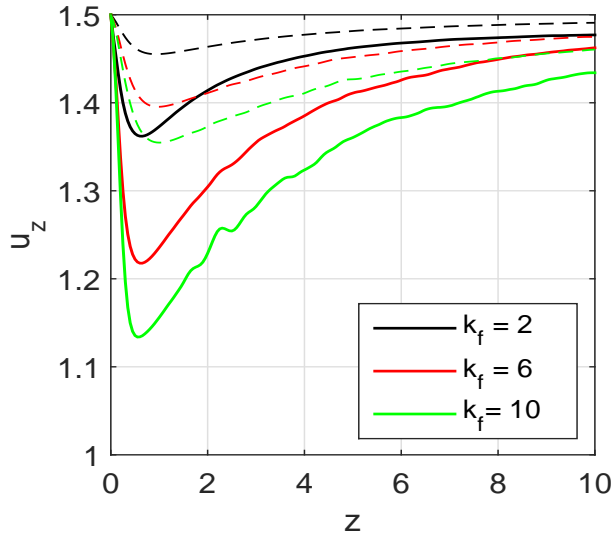


Figure 15: Fibre suspension flow through a circular tube: the centreline velocity profiles of flows with  $k_f = \{2, 6, 10\}$  (solid lines). The corresponding results for the fibre suspension flow between two parallel plates presented in section 7.1 are also reproduced in dashed-line form for comparative purpose.

Table 2: Fibre suspension flow through a circular tube. Value and distance from the inlet boundary of undershoots appearing in the centreline velocity profiles with  $k_f = \{2, 6, 10\}$ . Results for planar flows are included for comparative purpose.

	$k_f$	Undershoot value	Undershoot's position
Flow through a circular tube	2	1.362	$z = 0.65$
	6	1.2177	$z = 0.65$
	10	1.1338	$z = 0.55$
Flow between two parallel plates	2	1.4552	$x = 0.95$
	6	1.3954	$x = 0.95$
	10	1.3547	$x = 1$

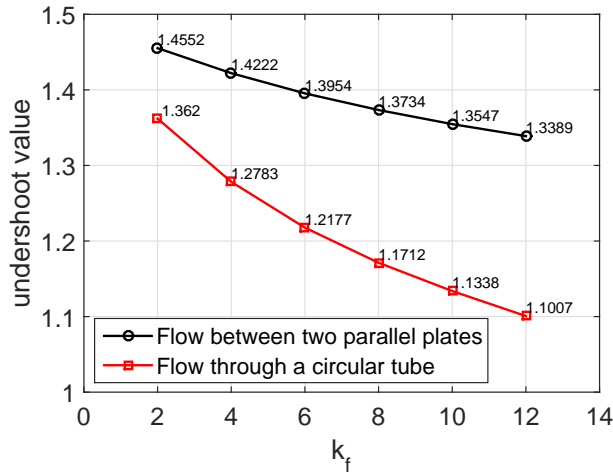


Figure 16: Fibre suspension flow through a circular tube: the undershoot value of the centreline velocity profiles for the fibre suspension flows with  $k_f = \{2, 4, 6, 8, 10, 12\}$ . The corresponding results of the flow between two parallel plates are also presented here for comparative purpose.

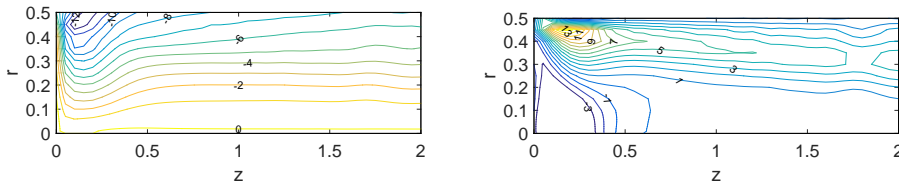


Figure 17: Fibre suspension flow through a circular tube: the distribution of shear stress (left figure) and the first normal stress difference (right figure) for the case of fibre parameter  $k_f = 10$ .

Fig. 17 depicts the shear stress and the first normal stress difference of the suspension flow through a circular tube with the fibre parameter  $k_f = 10$ . The distribution of shear stress presented in Fig. 17 (left figure) shows that there is no significant difference in comparison with the one by the suspension flow between two parallel plates (Fig. 10 - left figure). Furthermore, a maximum shear stress of 12 was also observed near the corner of the inlet and the wall boundaries. Meanwhile there is only a small difference in the first normal stress difference distribution between the two suspension flows: a distribution of the first normal stress difference  $[-3, 13]$  (Fig. 17 - right figure) for the flow through a circular tube versus  $[-2, 11]$  (Fig. 10 - right figure) for the flow between two parallel plates.

7.3 Fibre suspension flow through 4 : 1 and 4.5 : 1 axisymmetric contractions

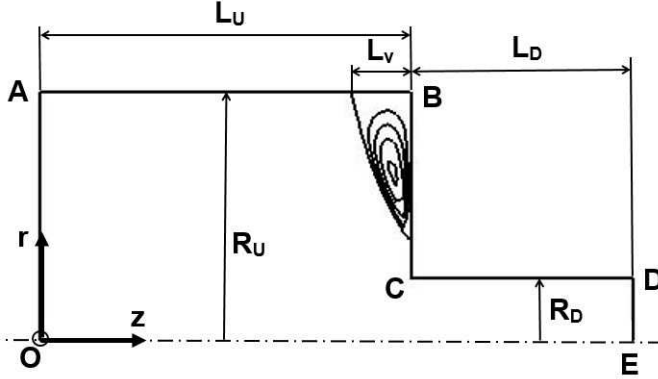


Figure 18: Fibre suspension flow through an axisymmetric contraction: A schematic geometry for the 4 : 1 and 4.5 : 1 axisymmetric contraction flows.

The geometry of the axisymmetric contraction problem presented in Fig. 18 was considered by Chiba, Nakamura, and Boger (1990) where  $L_U = 5$  and  $R_U = 1$  are the length and radius of the upstream tube;  $L_D = 3$  and  $R_D = 0.25$  the length and radius of the downstream tube and  $L_v$  the vortex length at the upstream corner. For the 4.5 : 1 contraction flow, the radius of the upstream tube is increased to  $R_U = 1.125$  while the other geometry parameters are the same.

The contraction ratio  $\beta$  and the dimensionless vortex length  $L_v^*$  of the problem are defined, respectively, as follows.

$$\beta = \frac{R_U}{R_D}, \quad L_v^* = \frac{L_v}{2R_U}. \tag{61}$$

A non-uniform grid used in the simulation is described in Fig. 19. A finer grid are generated to capture sufficiently the values of field variables in the contraction area where the variable gradients are very steep. Furthermore, the axial velocity in the area close to the centreline cannot be calculated using  $u_z = \frac{1}{r} \frac{\partial \Psi}{\partial r}$  because of the singularity. In order to avoid this issue,  $u_z$  is approximated as  $\lim_{r \rightarrow 0} \frac{1}{r} \frac{\partial \Psi}{\partial r} = \frac{\partial^2 \Psi}{\partial r^2}$  (L'Hospital rule) on the centreline. Therefore, a finer mesh is installed near the centreline. A detailed cartesian grid is generated as follows.  $\Delta z_1 = 0.05, \forall z \in [4, 6]$  and  $\Delta z_2 = 0.1, \forall z < 4 \cup z > 6$ ; and  $\Delta r_1 = 0.01, \forall r \in [0, 0.1]$  and  $\Delta r_2 = 0.025, \forall r > 0.1$ . The time step size is chosen as  $5E-4$ .

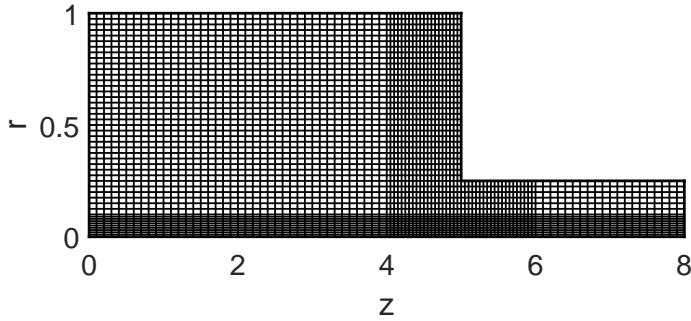


Figure 19: Fibre suspension flow through an axisymmetric contraction: a non-uniform Cartesian grid for the 4 : 1 axisymmetric contraction flow.

### 7.3.1 Governing equations and boundary conditions

The fibre suspension flow through an axisymmetric contraction is governed by Eqs. (52) - (60) with the following boundary conditions (see Fig. 18).

- At the inlet  $\overline{OA}$ : The velocity profile and the corresponding stream function and vorticity at the inlet are obtained from the solution of the fibre suspension flow through circular tube with the same parameters of the fluid as presented in section 7.2 (We use a length to diameter ratio of 30 to obtain a fully developed velocity profile). Furthermore,  $\frac{\partial \Psi}{\partial z} = 0$  is also imposed;
- At the outlet  $\overline{DE}$ : The flow-out boundary condition is defined by  $\frac{\partial u_z}{\partial z} = 0$  and  $u_r = 0$ ;  $\frac{\partial \Psi}{\partial z} = 0$ ; and  $\frac{\partial \omega}{\partial z} = 0$ ;
- On the walls  $\overline{AB}$ ,  $\overline{CD}$  and  $\overline{BC}$ : The non-slip boundary condition is imposed for the velocity:  $u_z = 0$  and  $u_r = 0$ . Hence, the corresponding boundary conditions for the stream function and the vorticity on the walls are given as follows.

– On the wall  $\overline{AB}$ :

$$\Psi = 0, \quad \frac{\partial \Psi}{\partial r} = 0;$$

$$\omega = \omega_{w1};$$

– On the wall  $\overline{CD}$ :

$$\Psi = 0, \quad \frac{\partial \Psi}{\partial r} = 0;$$

$$\omega = \omega_{w3};$$

– On the wall  $\overline{BC}$ :

$$\Psi = 0, \quad \frac{\partial \Psi}{\partial z} = 0;$$

$$\omega = \omega_{w_2},$$

where  $\omega_{w_1}$ ,  $\omega_{w_2}$  and  $\omega_{w_3}$  are determined and updated using Eq. (53) with the known stream function at each time step;

• On the centreline  $\overline{OE}$ :

- The symmetric boundary condition of the velocity field is applied, i.e.  $\frac{\partial u_z}{\partial r} = 0$  and  $u_r = 0$ ;
- The corresponding boundary conditions for the stream function and the vorticity are given by

$$\Psi = \Psi_c, \quad \frac{\partial \Psi}{\partial r} = 0;$$

$$\omega = 0,$$

where  $\Psi_c$  is determined by Eq. (54) using the inlet boundary condition of the velocity.

### 7.3.2 Results and discussion

A range of fibre parameters and Reynolds numbers is used to simulate the two challenging 4 : 1 and 4.5 : 1 axisymmetric contraction flow problems by the present method. The number of fibre configuration fields used in all cases is  $N_f = 1000$ . Results obtained by the present method are in very good agreement with those of Chiba, Nakamura, and Boger (1990) or Lipscomb, Denn, Hur, and Boger (1988). Results are detailed and discussed as follows.

The 4 : 1 contraction flow is simulated with a range of fibre parameters  $k_f = \{0, 1, \dots, 11, 12\}$  for  $Re = 0$  (the creeping flow);  $k_f = \{0, 1, \dots, 7, 8\}$  for  $Re = 1$ ; and  $k_f = 6$  for  $Re = 2$  and  $Re = 5$ . Fig. 20 presents the effect of the fibre parameter ( $k_f$ ) on the vortex length for the flows with  $Re = 0$  and  $Re = 1$ . Results showed insignificant differences on the vortex length by the present method and the publication in Chiba, Nakamura, and Boger (1990). For example, for the creeping fibre suspension flow ( $Re = 0$ ), while the vortex length is 0.170 by the experiment mentioned in (Chiba, Nakamura, and Boger, 1990), it is approximately 0.160 and 0.175 by (Chiba, Nakamura, and Boger, 1990) using the Finite Different Method and the present method, respectively. Furthermore, the vortex lengths by our present method are slightly higher for  $k_f < 5$  but a bit lower for  $k_f > 5$  than those of Chiba, Nakamura, and Boger (1990) for creeping fibre suspension flows, whereas the

obtained results by the present work and from Chiba, Nakamura, and Boger (1990) are nearly the same for the flows with  $Re = 1$ .

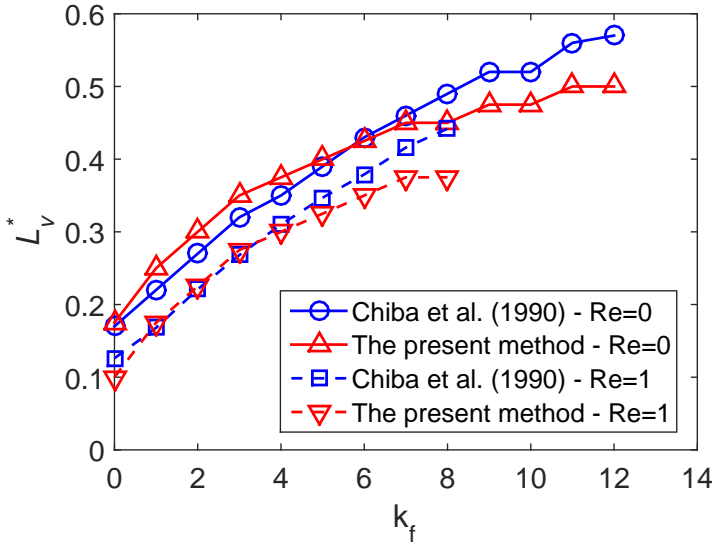


Figure 20: The axisymmetric 4 : 1 contraction flows of fibre suspensions: the effect of the fibre parameter on the vortex length ( $L_v^*$ ) with a range of  $k_f = \{0, 1, \dots, 11, 12\}$  for the flows with  $Re = 0$  and  $k_f = \{0, 1, \dots, 7, 8\}$  for the flows with  $Re = 1$ .

Effect of the fibre suspension on the development of the salient corner vortex is clearly reflected in Fig. 21. As compared with the Newtonian fluid flow ( $k_f = 0$  - top left figure) the size of the salient corner vortex of fibre suspension flows gradually grows with increasing fibre parameter. Furthermore, due to the impact by the growing vortex, the gradient of streamlines close to the contraction area reduces with increasing fibre parameter. Results shown in Fig. 21 by the present work are in very good agreement with those of Chiba, Nakamura, and Boger (1990). However, a minor difference has been found in our present work in comparison with others (Chiba, Nakamura, and Boger, 1990; Lipscomb, Denn, Hur, and Boger, 1988; Lu, Khoo, Dou, Phan-Thien, and Seng Yeo, 2006) in the form of a small secondary vortex at the upstream corner of the contraction as shown in Fig. 21. This result may indicate that the present method is capable of capturing such fine details.

Fig. 22 depicts the effect of the fibre parameter on the fibres orientation around the contraction area. It can be recognised that fibres tend to align with the flow direction when approaching the contraction region. The fibres are mostly parallel

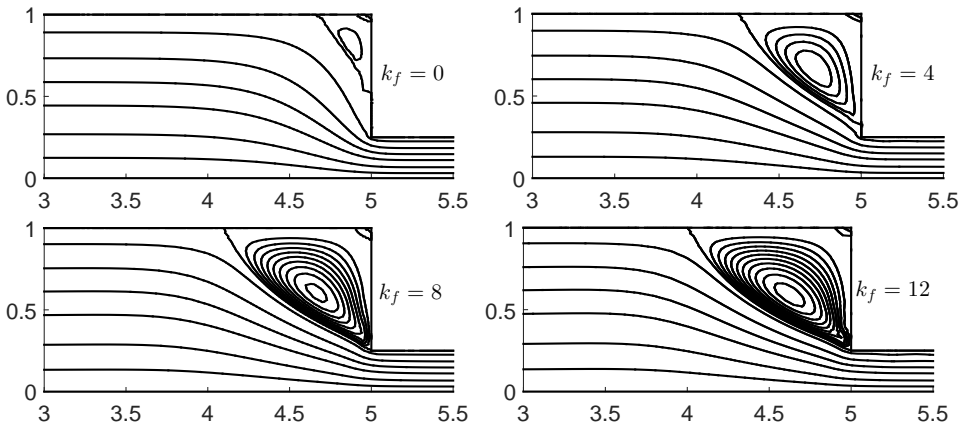


Figure 21: The axisymmetric 4 : 1 contraction flows of fibre suspensions: the effect of the fibre parameter on the streamlines and the vortex of the velocity field for the flows with  $Re = 0$  and a range of  $k_f = \{0, 4, 8, 12\}$ .

with the flow direction in the downstream due to the impact of the elongation of the fluid. This tendency is more pronounced with increasing fibre parameter.

The effect of Reynolds number on the contraction flow of fibre suspensions was also investigated and presented in Fig. 23 with a range of  $Re = \{0, 1, 2, 5\}$  with  $k_f = 6$ . In contrast to the effect of the fibre parameter (Fig. 21), the salient corner vortex diminishes in size as the Reynolds number increases as stated and explained by Chiba, Nakamura, and Boger (1990).

Fig. 24 describes the axial velocity profile along the centreline of fibre suspension flows with a range of  $k_f = \{0, 4, 8, 12\}$  and  $Re = 0$ . Unlike the case of a viscoelastic fluid, where an overshoot of the velocity profile on the centreline appears near the contraction area (Marchal and Crochet, 1987), it was not observed in the fibre suspension flows. This result was previously confirmed by Chiba, Nakamura, and Boger (1990); Baloch and Webster (1995). Furthermore, results presented in Fig. 24 showed that the axial velocity at the far upstream and far downstream of the flow does not significantly change with the fibre parameter while the velocity gradient increases, with the decrease of the fibre parameter, around the contraction region (Fig. 25). This increment of the velocity gradient reaches a maximum peak value (65) with the case of Newtonian fluid ( $k_f = 0$ ).

The first normal stress difference ( $\tau_e^{zz} - \tau_e^{rr}$ ) of the fibre suspension flow on the centreline is finally determined by the following expression of Chiba, Nakamura,

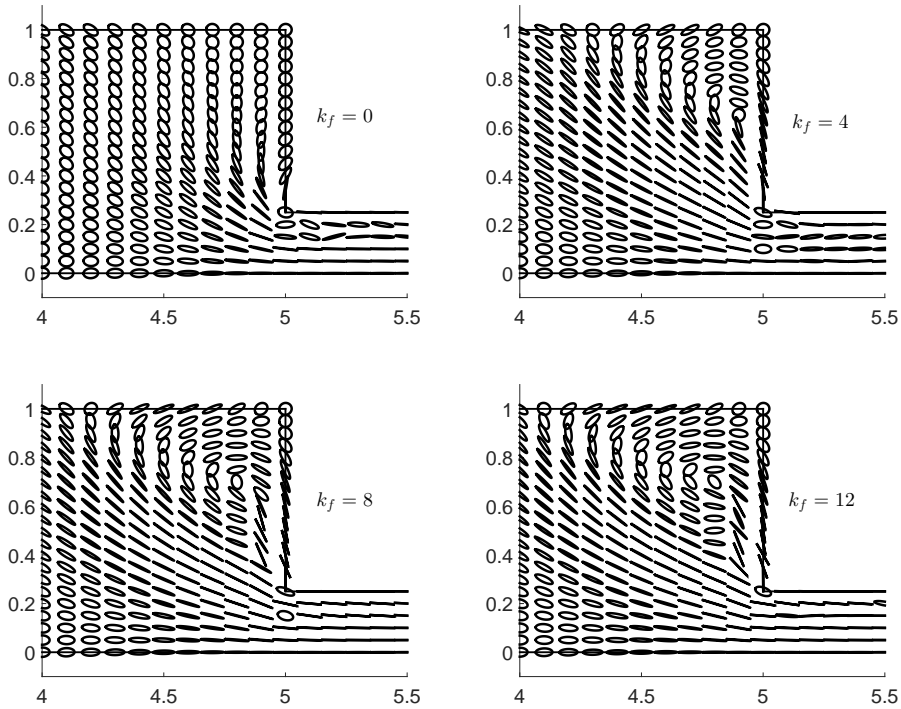


Figure 22: The axisymmetric 4 : 1 contraction flows of fibre suspensions: the distribution of the fibres' orientation around the contraction area for the flows with  $Re = 0$  and a range of  $k_f = \{0, 4, 8, 12\}$ .

and Boger (1990)

$$\tau_e^{zz} - \tau_e^{rr} = 2\left(\frac{\partial u_z}{\partial z} - \frac{\partial u_r}{\partial r}\right) + k_f \frac{\partial u_z}{\partial z}, \quad (62)$$

where the first and second terms of the RHS are the Newtonian solvent contribution and the fibre stress contribution to the first normal stress difference of the fibre suspension flow, respectively. Fig. 26 depicts the first normal stress difference which gradually increases and reaches a peak value at the position just before the contraction region of the upstream. Furthermore, the first normal stress difference together with its peak value increase with increasing fibre parameter. In other words, the first normal stress difference along the centreline is smallest for the Newtonian fluid where fibre stress contribution is non-existent (black line, Fig. 26).

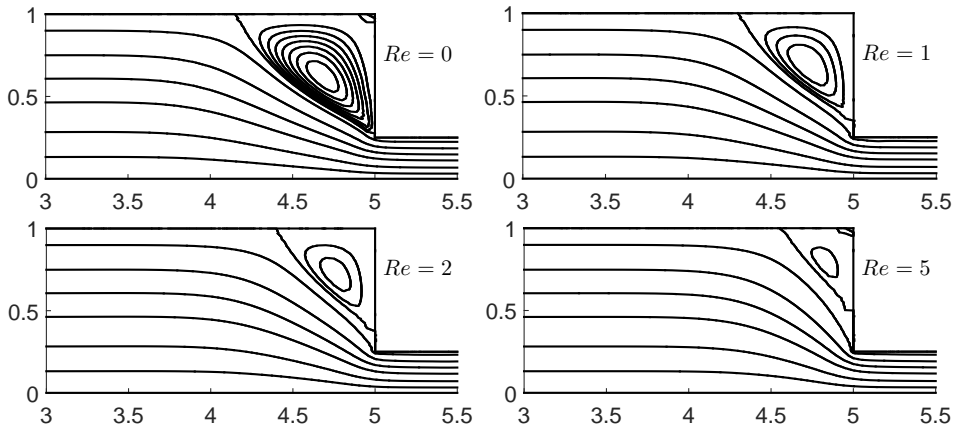


Figure 23: The axisymmetric 4 : 1 contraction flows of fibre suspensions: the effect of Reynolds number on the streamlines and vortices of the velocity field for a range of  $Re = \{0, 1, 2, 5\}$  and  $k_f = 6$ .

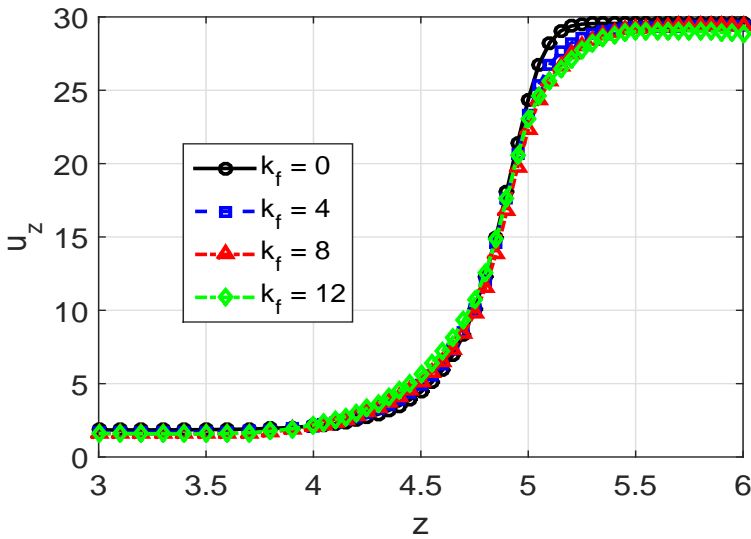


Figure 24: The axisymmetric 4 : 1 contraction flows of fibre suspensions: The axial velocity profile on the centreline for a range of  $k_f = \{0, 4, 8, 12\}$  and  $Re = 0$ .

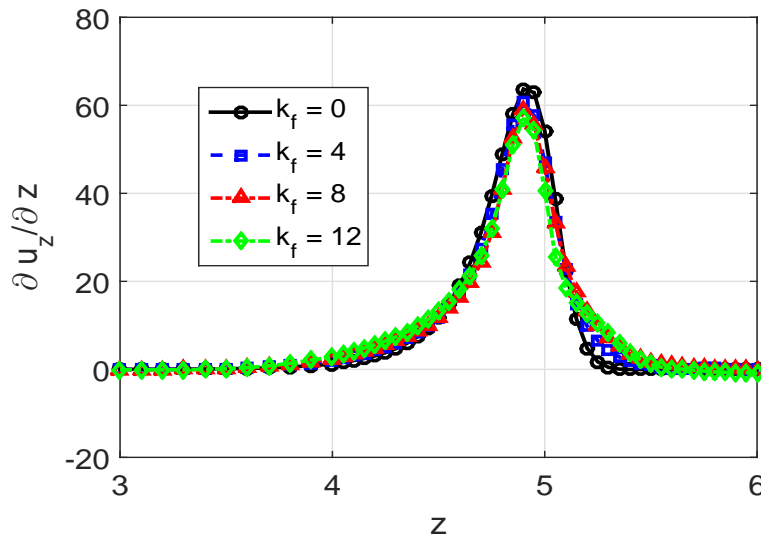


Figure 25: The axisymmetric 4 : 1 contraction flows of fibre suspensions: The velocity gradient profile on the centreline for a range of  $k_f = \{0, 4, 8, 12\}$  and  $Re = 0$ .

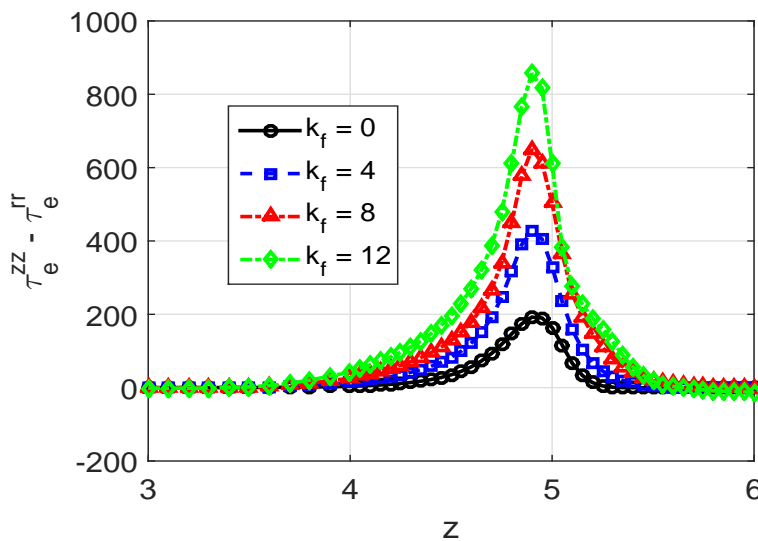


Figure 26: The axisymmetric 4 : 1 contraction flows of fibre suspensions: The first normal stress difference on the centreline for a range of  $k_f = \{0, 4, 8, 12\}$  and  $Re = 0$ .

Finally, the 4.5 : 1 contraction flow of fibre suspensions is simulated with range of  $k_f = \{0, 1, \dots, 7, 8\}$  and  $Re = 0$ . The problem was previously investigated by both experiment and the finite element method in Lipscomb, Denn, Hur, and Boger (1988). Fig. 27 describes the effect of the fibre parameter on the length of vortex at the contraction corner. The figure shows that the results by the present method are comparable with the experimental ones and in very good agreement with the numerical ones presented by Lipscomb, Denn, Hur, and Boger (1988).

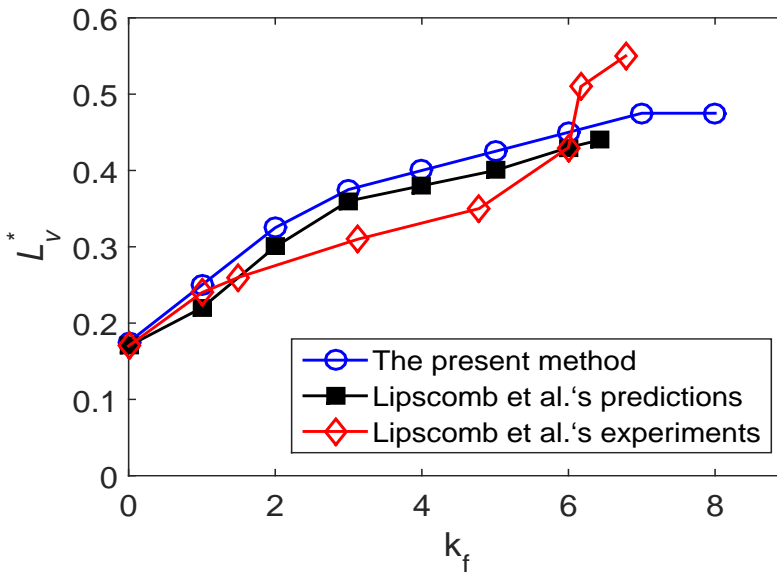


Figure 27: The axisymmetric 4.5 : 1 contraction flows of fibre suspensions: the effect of the fibre parameter on the vortex length ( $L_v^*$ ) for a range of  $k_f = \{0, 1, \dots, 7, 8\}$  and  $Re = 0$ .

## 8 Conclusions

This paper reports the use of a multiscale method based on the fibre configuration field, the 1D-IRBF scheme and the DAVSS technique to simulate dilute fibre suspension flows. In this new approach, at each time step, the governing differential equations, including the stream function and vorticity transport equations, are spatially discretised using the 1D-IRBF method. Meanwhile, the evolution of fibre configurations governed by Jeffery's equation are approximated using the BCF principle. The two scales are linked together by the Lipscomb's model, which is

applied to calculate the fibre stress tensor for dilute suspensions. In addition, the adoption of the DAVSS enhances the numerical stability of the 1D-IRBF based scheme in simulating fibre suspension flow problems. As a result, the efficiency of the present approach is significantly increased as stated in section 7. Indeed, the obtained results of the simulation of fibre suspension flows through the challenging 4 : 1 and 4.5 : 1 axisymmetric contraction geometries may indicate that the present approach is capable of capturing such fine details as secondary vortices in the corners.

**Acknowledgement:** The first author would like to thank the University of Southern Queensland for a Postgraduate Research scholarship and Scholarship Supplements by the Faculty of Health, Engineering and Sciences and the Computational Engineering and Science Research Centre. These supports are gratefully acknowledged. We would like to thank the reviewers for their helpful comments.

## References

**Advani, S. G.; Tucker III, C. L.** (1987): The use of tensors to describe and predict fiber orientation in short fiber composites. *Journal of Rheology*, vol. 31, no. 8, pp. 751–784.

**Baloch, A.; Webster, M. F.** (1995): A computer simulation of complex flows of fibre suspensions. *Computers & Fluids*, vol. 24, no. 2, pp. 135–151.

**Chiba, K.; Nakamura, K.; Boger, D. V.** (1990): A numerical solution for the flow of dilute fiber suspensions through an axisymmetric contraction. *Journal of Non-Newtonian Fluid Mechanics*, vol. 35, no. 1, pp. 1–14.

**Chiba, K.; Yasuda, K.; Nakamura, K.** (2001): Numerical solution of fiber suspension flow through a parallel plate channel by coupling flow field with fiber orientation distribution. *Journal of Non-Newtonian Fluid Mechanics*, vol. 99, no. 2, pp. 145–157.

**Dong, L.; Atluri, S. N.** (2012): Development of 3D T-Trefftz Voronoi Cell Finite Elements with/without spherical voids and/or elastic/rigid inclusions for micromechanical modeling of heterogeneous materials. *CMC: Computers, Materials & Continua*, vol. 29, no. 2, pp. 169–211.

**Dong, L.; Atluri, S. N.** (2013): SGBEM Voronoi Cells (SVCs), with embedded arbitrary-shaped inclusions, voids, and/or cracks, for micromechanical modeling of heterogeneous materials. *CMC: Computers, Materials & Continua*, vol. 33, no. 2, pp. 111–154.

**Dou, H.-S.; Khoo, B. C.; Phan-Thien, N.; Yeo, K. S.; Zheng, R.** (2007): Simulations of fibre orientation in dilute suspensions with front moving in the filling process of a rectangular channel using level-set method. *Rheologica Acta*, vol. 46, no. 4, pp. 427–447.

**Fan, X.-J.** (2006): *Numerical study on some rheological problems of fibre suspensions*. PhD thesis, The University of Sydney, 2006.

**Fan, X.-J.; Phan-Thien, N.; Zheng, R.** (1999): Simulation of fibre suspension flows by the Brownian configuration field method. *Journal of Non-Newtonian Fluid Mechanics*, vol. 84, no. 2, pp. 257–274.

**Fan, X.-J.; Phan-Thien, N.; Zheng, R.** (2000): Simulation of fibre suspension flow with shear-induced migration. *Journal of Non-Newtonian Fluid Mechanics*, vol. 90, no. 1, pp. 47–63.

**Ferreira, V. G.; Tomé, M. F.; Mangiavacchi, N.; Castelo, A.; Cuminato, J. A.; Fortuna, A. O.; McKee, S.** (2002): High-order upwinding and the hydraulic jump. *International Journal for Numerical Methods in Fluids*, vol. 39, no. 7, pp. 549–583.

**Folgar, F.; Tucker, C. L.** (1984): Orientation behavior of fibers in concentrated suspensions. *Journal of Reinforced Plastics & Composites*, vol. 3, no. 2, pp. 98–119.

**Folkes, M.** (1982): *Short Fibre Reinforced Thermoplastics*. Research Studies Press, Wiley: New York.

**Hulsen, M. A.; Van Heel, A. P. G.; Van Den Brule, B. H. A. A.** (1997): Simulation of viscoelastic flows using Brownian configuration fields. *Journal of Non-Newtonian Fluid Mechanics*, vol. 70, no. 1, pp. 79–101.

**Jeffery, G. B.** (1922): The motion of ellipsoidal particles immersed in a viscous fluid. *Proceedings of the Royal Society of London. Series A, Containing papers of a mathematical and physical character*, pp. 161–179.

**Lipscomb, G. G.; Denn, M. M.; Hur, D. U.; Boger, D. V.** (1988): The flow of fiber suspensions in complex geometries. *Journal of Non-Newtonian Fluid Mechanics*, vol. 26, no. 3, pp. 297–325.

**Lu, Z.; Khoo, B. C.; Dou, H.-S.; Phan-Thien, N.; Seng Yeo, K.** (2006): Numerical simulation of fibre suspension flow through an axisymmetric contraction and expansion passages by Brownian configuration field method. *Chemical Engineering Science*, vol. 61, no. 15, pp. 4998–5009.

**Mai-Duy, N.; Le-Cao, K.; Tran-Cong, T.** (2008): A Cartesian grid technique based on one-dimensional integrated radial basis function networks for natural con-

vection in concentric annuli. *International Journal for Numerical Methods in Fluids*, vol. 57, no. 12, pp. 1709–1730.

**Marchal, J. M.; Crochet, M. J.** (1987): A new mixed finite element for calculating viscoelastic flow. *Journal of Non-Newtonian Fluid Mechanics*, vol. 26, no. 1, pp. 77–114.

**Nguyen, H. Q.; Tran, C. D.; Tran-Cong, T.** (2015): RBFN stochastic coarse grained simulation method: Part I - Dilute polymer solutions using Bead-Spring Chain models. *CMES: Computer Modeling in Engineering & Sciences*, vol. 105, pp. 339–439.

**Phan-Thien, N.; Graham, A. L.** (1991): A new constitutive model for fibre suspensions: flow past a sphere. *Rheologica Acta*, vol. 30, no. 1, pp. 44–57.

**Phan-Thien, N.; Graham, A. L.; Altobelli, S. A.; Abbott, J. R.; Mondy, L. A.** (1995): Hydrodynamic particle migration in a concentrated suspension undergoing flow between rotating eccentric cylinders. *Industrial & Engineering Chemistry Research*, vol. 34, no. 10, pp. 3187–3194.

**Sun, J.; Phan-Thien, N.; Tanner, R. I.** (1996): An adaptive viscoelastic stress splitting scheme and its applications: AVSS/SI and AVSS/SUPG. *Journal of Non-Newtonian Fluid Mechanics*, vol. 65, no. 1, pp. 75–91.

**Sun, J.; Smith, M. D.; Armstrong, R. C.; Brown, R. A.** (1999): Finite element method for viscoelastic flows based on the discrete adaptive viscoelastic stress splitting and the discontinuous Galerkin method: DAVSS-G/DG. *Journal of Non-Newtonian Fluid Mechanics*, vol. 86, no. 3, pp. 281–307.

**Tran, C. D.; An-Vo, D. A.; Mai-Duy, N.; Tran-Cong, T.** (2011): An integrated RBFN-based macro-micro multi-scale method for computation of visco-elastic fluid flows. *CMES: Computer Modeling in Engineering & Sciences*, vol. 82, no. 2, pp. 137–162.

**Tran, C. D.; Mai-Duy, N.; Le-Cao, K.; Tran-Cong, T.** (2012): A continuum-microscopic method based on IRBFs and control volume scheme for viscoelastic fluid flows. *CMES: Computer Modeling in Engineering & Sciences*, vol. 85, no. 6, pp. 499–519.

**Tran, C. D.; Phillips, D. G.; Tran-Cong, T.** (2009): Computation of dilute polymer solution flows using BCF-RBFN based method and domain decomposition technique. *Korea-Australia Rheology Journal*, vol. 21, no. 1, pp. 1–12.

**Tran-Canh, D.; Tran-Cong, T.** (2004): Element-free simulation of dilute polymeric flows using Brownian Configuration Fields. *Korea-Australia Rheology Journal*, vol. 16, no. 1, pp. 1–15.

**Wu, Y. T.; Nie, Y. F.; Yang, Z. H.** (2014): Comparison of four multiscale methods for elliptic problems. *CMES: Computer Modeling in Engineering & Sciences*, vol. 99, no. 4, pp. 297–325.

